COMPUTATIONAL FLUID FLOW AND TRANSPORT OF COLLOIDAL PARTICLES IN SOIL PORES

A Dissertation

Presented to the Faculty of the Graduate School

of Cornell University

In Partial Fulfillment of the Requirements for the Degree of

Doctor of Philosophy

by

Mehmet Ekrem Cakmak

January 2011

COMPUTATIONAL FLUID FLOW AND TRANSPORT OF COLLOIDAL PARTICLES IN SOIL PORES

Mehmet Ekrem Cakmak, Ph. D.

Cornell University 2011

Transport of colloidal size particulate matter is of special interest of environmental studies because colloids and adsorbed chemicals can be transported over long distances. Colloid facilitated transport can pose potentially high risk for pollution of ground water. Visualizations of colloid transport using bright field and confocal microscopes have discovered interesting phenomena such colloids moving in circles that cannot be described by the traditional Darcy scale models. That is why computational pore scale models are needed to better understand colloid transport and fate in porous media. Transport and fate of colloids depend largely on flow field in the pores and it is, therefore, important to simulate the flow field while taking grain surface properties into account. The aim of this dissertation is hence to determine the flow fields in realistic pores by solving the incompressible Navier-Stokes equation with a powerful commercial available finite element program COMSOL Multiphysics. The dissertation has five chapters. In the first chapter a short introduction is given. In the second chapter the COMSOL Multiphysics program is tested by revisiting the classical colloid filtration theory on colloid retention on a spherical sand grain. Retention of colloids on grains simulated with COMSOL is found to be similar to semi-analytical solutions previously published. Subsequently colloid retention on an air bubble is simulated and greater colloid retention is calculated than on a soil grain

due to the slip boundary condition at the Air-Water interface which creates higher velocities and more fluid flow around air bubble resulting in greater amounts of colloids that can diffuse to the interface. In the third chapter the effect of surface roughness on hydrodynamics of colloid transport in a saturated porous media is investigated by simulating the flow fields around perfectly smooth, smoothed, and naturally rough sand grains. The results show that micron scale surface asperities of rough grains create greater vorticity and more stagnant flow regions compared to smooth grains likely resulting in greater colloid retention for the rough grains. In the fourth chapter the dependence of dynamic contact angle between the interface of two immiscible fluids and solid surface on the interface velocity is simulated in an empty capillary channel to provide a new understanding on the formation of unstable wetting fronts in coarse or water repellent soils. The results show an increase in contact angle when the velocity of the front increases, which is consistent with experimental studies in the literature. In the fifth chapter the problems encountered during the research and future directions are briefly explained.

BIOGRAPHICAL SKETCH

After getting a B.S. degree in Environmental Engineering from Mersin University (Turkey) in 2002, Mehmet Ekrem Cakmak received a M.S. degree from the Department of Environmental Engineering at Cukurova University (Turkey) in 2004. From there Ekrem was admitted as a PhD student in Biological and Environmental Engineering at Cornell University in January 2005. At Cornell, Ekrem was part of Soil and Water Group under Tammo S. Steenhuis.

ACKNOWLEDGMENTS

I would like to acknowledge the many individuals who provided assistance, support and guidance during my studies at Cornell. First and foremost, I would like to express my sincere gratitude to my advisor and special committee chair, Professor Tammo S. Steenhuis, for all his support, guidance, encouragement, and supervision. My sincere gratitude also goes to Professors J. Yves Parlange, Anthony G. Hay, and John L. Nieber my committee members for their patience, inputs and suggestions in the preparation of this dissertation. Second, I would like to thank Dr. Ahmet YUCEER, Dr. Mesut Basibuyuk, Dr. Fuat Budak, Dr. Zeynep Zaimoglu, and Dr. Hasan R. Kutlu from Cukurova University, Turkey, who have always helped and motivated me in my graduate studies.

I am very thankful to Yuniati Zevi, Veronica L. Morales, Daniel Fuka, Wei Zhang, and Anthony Salvucci for their suggestions, comments, and helps associated with my research. I am grateful to Dr. Brian K. Richards for his support and help in Soil and Water Group. I would like to thank all my colleagues in Soil and Water Group for the memorable moments and enjoyable work space. And, of course, I would like to thank my family and friends for their love, support, and patience.

Finally, I would like to thank the Higher Education Council of Turkey and Cukurova University (Adana, TURKEY) for the Scholarship fund that financed my work for the first 4 years at Cornell University. I would like to acknowledge partial financial supports by NSF (51674/A001), USDA (48718/A001) and BARD funds.

TABLE OF CONTENTS

LIST OF FIGURES

LIST OF TABLES

CHAPTER 1
INTRODUCTION

This dissertation consists of three manuscripts.

Chapter 2 reexamines the classical colloid filtration theory that on colloid retention efficiency in a saturated porous medium by the colloid retention efficiency of a single spherical sand grain in a pore space that reflects the porosity of whole porous medium. After validating our results with the results of previous studies the colloid retention efficiency of an air bubble is investigated to purpose a simulation base for unsaturated porous medium. Relatively high retention of colloids on the air bubble surface is found because of high fluid flow velocity tangential to the air bubble surface.

In Chapter 3 the effect of micron scale surface roughness of soil grains on hydrodynamics of colloid transport is examined. Fluid flow over perfectly smooth, smoothed, and naturally rough soil grain surfaces were simulated. The results show that micron scale surface asperities result in the formation of vorticities and stagnant flow regions near the grain surface. As expected more vorticities are found for naturally rough soil grains than for smoothed surfaces.

In Chapter 4, the dynamic behavior of wetting front in a capillary channel was simulated. The effect of wetting front velocity on the dynamic contact angle was validated against experimental results of previous studies. Similarly to previous studies an increase of dynamic contact angle with increasing contact line velocity was observed.

CHAPTER 2
PORE SCALE SIMULATION OF COLLOID DEPOSITION

2.1. INTRODUCTION

Mobile subsurface colloids have received considerable attention because the migration of colloids and colloid-contaminant complexes through the solid matrix substantially increase the risk of groundwater pollution. Typically defined as suspended particulate matter with diameter less than 10μm, colloids include both organic and inorganic materials such as microorganisms, humic substances, clay minerals and metal oxides. Accurate prediction of the fate of colloids is important to predict colloid facilitated transport of pollutants, and the transport of biocolloids such as viruses and bacteria. In colloid transport studies colloid deposition, that is, the capture of colloids by grain surfaces, is considered as the primary mechanism controlling the transport of colloids in groundwater [*Ryan and Elimelech,* 1996]. The role of electrostatic and hydrodynamic forces in controlling colloid deposition behavior of colloids has been afforded detailed investigation in the field of colloid science to gain more understanding about colloid-surface interaction processes. The study of deposition rates of colloids onto model collectors has provided substantial information on the electrostatic and hydrodynamic forces involved in the transport of colloids [*Elimelech et al.,* 1995; *Tien and Ramarao,* 2007]. Most of these studies have focused on colloid transport under saturated conditions [*Keller and Auset,* 2007; *Rajagopalan and Tien,* 1976; *Ryan and Elimelech,* 1996; *Yao et al.,* 1971]. However, there is not much information available on colloid behavior under unsaturated conditions due to the complexity of the conditions involved [*Auset and Keller,* 2004; *Crist et al.,* 2005; *DeNovio et al.,* 2004; *Keller and Sirivithayapakorn,* 2004; *Keller and Auset,* 2007; *Zevi et al.,* 2005].

Most of the experimental and modeling studies on colloid transport under unsaturated conditions have focused primarily on colloid concentration in drainage water with very little emphasis on the precise mechanisms retaining the colloids in the pores [*Corapcioglu and Choi*, 1996; *DeNovio et al.*, 2004; *Lenhart and Saiers*, 2002]. Generally, the approaches used to simulate colloid transport can be classified into two types, Lagrangian or Eulerian. The Lagrangian approach focuses on the movement of distinct particles and tracks particle position in a moving fluid [*Rajagopalan and Tien*, 1976]. In contrast, the Eulerian approach considers the concentration distribution of particles in a porous media [*Tufenkji and Elimelech*, 2004; *Yao et al.*, 1971]. The Eulerian approach has advantages over the Lagrangian approach, in that it does not require high computational performance, and it is easy to incorporate Brownian motion [*Nelson and Ginn*, 2005; *Ryan and Elimelech*, 1996].

The deposition of colloids in porous media has been investigated by several researchers to improve existing methods by incorporating the forces such as hydrodynamic and attractive forces into the governing equations [*Rajagopalan and Tien*, 1976; *Tufenkji and Elimelech*, 2004; *Yao et al.*, 1971]. For instance, *Yao et al.* [1971] developed colloid filtration theory as a method for predicting colloid deposition in saturated porous media. A limitation of these studies is that the colloid transport and deposition simulations have been performed only for saturated media consisting of clean and spherical solid grains (collectors). These limitations led us to find a method to simulate colloid transport under unsaturated conditions where the air phase comes into play in addition to solid grains and moving water. This may be partly accomplished by modifying existing methods developed for saturated conditions. The main difficulty in more complex calculations is that the simulation methods are cumbersome, usually slow and cannot capture the complex pore geometries that exist in nature. That is why an effective, reliable, user-friendly and easy to be modified

simulation software is very important and needed in the modeling and simulation studies.

The objective for this chapter is to illustrate a test of the suitability of a finite element based computational modeling and simulation software package named COMSOL Multiphysics® (COMSOL, Inc., Burlington, MA, USA), for simulating colloid deposition on solid grains and air bubbles for conditions where Brownian motion dominates.

In the first part of the chapter we compare the COMSOL finite element solution with the analytical solutions of *Yao et al.* [1971], *Rajagopalan and Tien* [1976], and *Tufenkji and Elimelech* [2004] of classical filtration theory for one grain of a porous media. The second part involves the simulation of colloid deposition onto an inert air bubble.

2.2. COLLOID FILTRATION THEORY

In colloid filtration theory, the deposition efficiency of a porous medium is represented by the deposition efficiency of a unit collector, i.e. an isolated solid grain [*Rajagopalan and Tien*, 1976; *Tufenkji and Elimelech*, 2004; *Yao et al.*, 1971]. It is assumed that the porous medium is represented by an assemblage of perfect spherical solid grains (collectors). According to the theory, the transport of suspended colloids in the pore fluid to the vicinity of a stationary collector (i.e. a solid grain) is typically governed by three mechanisms: interception, gravitational settling, and Brownian diffusion. Interception takes place when the particles moving along the trajectories of flow streamlines come into contact with the collector due to the collector's finite size. Gravitational settling occurs when colloid particles have densities greater than the fluid density. These particles can then collide with a collector. The Brownian motion mechanism leads to diffusive migration of particles within a fluid and becomes

significant for particles smaller than 1 μm.

The transport of colloids is usually simulated by solving the convection-diffusion equation using a velocity field for the pore space between grains simulated with the Navier-Stokes equation for creeping flow conditions. The deposition of colloids from the fluid occurs by transfer of the colloids from the moving pore fluid onto the grain surface by the three aforementioned mechanisms. It is assumed that colloids do not accumulate on the grain surface, but that colloids 'disappear' once they are intercepted by the grain. The rate of overall particle deposition is found by integrating the particle flux over the collector surface. Within filtration theory it is also common to assume no colloid-colloid interaction, and that colloids do not affect the fluid flow.

The deposition of colloids onto a single grain has been simulated by *Yao et al.* [1971], *Rajagopalan and Tien* [1976], and *Tufenkji and Elimelech* [2004]. *Yao et al.* [1971] developed an equation to find the deposition efficiency of a unit collector by analytically solving the convection-diffusion equation based on the additivity assumption that allows the addition of the analytical solutions of each deposition mechanisms (interception, gravitational settling, and Brownian diffusion) independently [*Nelson and Ginn*, 2005]. They assumed that the collector existed in an infinite fluid stream with no interaction from surrounding collectors. For the same problem, *Rajagopalan and Tien* [1976] used the Lagrangian approach, (i.e., particle trajectory analysis) with boundary conditions for the flow field similar to *Happel* [1958]. These boundary conditions took into account the neighboring collectors as if the single (simulated) grain was located in a real porous media. Finally, *Tufenkji and Elimelech* [2004] developed a closed-form solution for calculating colloid deposition efficiency of a solid grain by combining the approaches of *Yao et al.* [1971] and *Rajagopalan and Tien* [1976].

2.3. SIMULATION METHODOLOGY

Since in addition to gravity effects, Brownian movement of colloids is of particular interest in the work presented here, the Eulerian colloid filtration theory originally developed by *Yao et al.* [1971] is chosen in our simulations. In this manuscript, the deposition of colloids on a single collector is simulated for the same boundary conditions as *Rajagopalan and Tien* [1976]. To find the velocity field the Navier-Stokes equations are solved with the finite element method. The resulting velocity field is then used in the solution to the convection-diffusion equation, with diffusion being due to Brownian motion of colloids and with gravitational settling included. In the next sections, the Navier-Stokes equation and the convection-diffusion equations are discussed both in general, and specifically how they are used in our simulations.

2.3.1. The Navier-Stokes Equations

The Navier-Stokes equations are employed to represent steady state creeping incompressible flow conditions, i.e.

$$-\frac{\partial p}{\partial i}+\mu\cdot\nabla^2 v_i+\rho_w g_i=0 \quad i=x,y,z$$
$$\nabla\cdot\underline{v}=0 \tag{2.1}$$

where p is the pressure (Pa), μ is the dynamic viscosity of the water (Pa.s), v_x, v_y, v_z are the vector components for the velocity ($\underline{v}=v_x\vec{i}+v_y\vec{j}+v_z\vec{k}$) of the water (m/s), ρ_w is the density of the water (kg/m^3), and g_x, g_y, g_z are the vector components for the gravitational acceleration (9.81 m/s^2). Equation (2.1) is valid for Reynolds number much less than one.

The Reynolds number is defined as

$$R_e=\frac{\underline{v}d\rho_w}{\mu} \tag{2.2}$$

where *d* is the diameter of the collector (m).

In a porous medium, fluid flow around a spherical collector is affected by the presence of other collectors around it. Therefore, a proper flow model for porous media is needed to reflect the disturbance of the flow field around the individual collectors. Among the various theoretical models Happel's fluid shell model is the most commonly used model [*Elimelech*, 1994; *Tien and Ramarao*, 2007]. Though the effect of neighboring collectors on fluid flow around the isolated unit collector is neglected in the original colloid filtration theory [*Yao et al.*, 1971], it is considered in this chapter by adopting Happel's model.

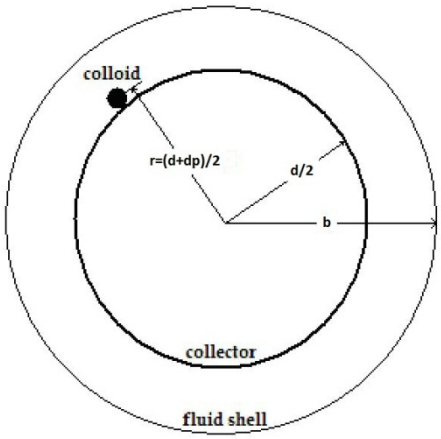

Figure 2.1. Schematic representation of a unit collector, and Happel's fluid shell

In Happel's model, the porous medium is constructed of identical spherical collectors, each of which is in a fluid shell (Fig. 2.1). In order to maintain the overall porosity of the porous medium for a single collector, the thickness of the shell, b, is defined as:

$$b = \frac{d}{2}(1-\varepsilon)^{-\frac{1}{3}} \tag{2.4}$$

where ε is the porosity of the porous medium.

The boundary conditions used in our simulations in the solution of the Navier-Stokes

equations can be summarized as follows. The surface of the fluid shell is specified as a symmetry boundary to take the effect of neighboring collectors on fluid flow into account. The symmetry boundary means that the velocity of the water normal to the boundary is zero at that boundary, and that the tangential component of the viscous force vanishes. A no-slip boundary condition is specified at the surface of the solid grain where the water velocity equals zero [*Spielman*, 1977; *Tien and Ramarao*, 2007]. Later we will consider the simulations for flow around a single air bubble, and for that case the surface of the bubble is specified to be a slip boundary [*Nguyen and Jameson*, 2005; *Shew and Pinton*, 2006].

2.3.2. Convection-Diffusion Equation

Once the velocity field is determined, the distribution of colloids within the pore space of a porous medium can be found by solving the convection-diffusion equation for steady state conditions [*Yao et al.*, 1971]. The convection-diffusion equation is given by

$$\left[\underline{v}\cdot\nabla C\right]-\left[D\ \cdot\nabla^2 C\right]-\sum_i\left[(1-\frac{\rho_w}{\rho_p})\ \frac{mg_i}{3\pi\mu d_p}\frac{\partial C}{\partial x_i}\right]=0 \qquad (2.5)$$

where C is the concentration of the colloids (number of colloids/m^3), D is the diffusion coefficient of the colloids calculated by Einstein's equation (m^2/s), ρ_p is the density of an individual colloid (kg/m^3), m is the mass of the colloids (kg), and d_p is the diameter of the colloids (m). The terms in the equation represent (left to right) the colloid transport processes of convection, diffusion, and gravitational settling.

When colloids make contact with a collector surface it is assumed that they disappear into the collector by specifying the collector surface as being a perfect sink. This means that all colloids arriving at the collector surface are irreversibly captured. The

condition for a perfect sink can be achieved by setting the concentration in the vicinity of the collector surface to zero, i.e.,

$$C = 0 \text{ at } r = (d+d_p)/2 \tag{2.6}$$

where *r* represents the radius of an imaginary spherical surface displaced slightly outward from the surface of the collector (m) (Figure 2.1).

At an infinite distance from the collector center the colloid concentration is assumed to be equal to the free stream concentration, C_0 [*Elimelech*, 1994; *Yao et al.*, 1971].

$$C = C_0 \text{ at } r = \infty \tag{2.7}$$

In previous analyses that used Happel's model for the flow velocity field, the above boundary condition is specified at the surface of the fluid shell, i.e.,

$$C = C_0 \text{ at } r = b \tag{2.8}$$

The diffusion coefficient in the convection-diffusion equation is calculated by Einstein's equation:

$$D = \frac{k\,T}{3\,\pi\,\mu\,d_p} \tag{2.9}$$

where *k* is the Boltzmann's constant (J/K), and *T* is the absolute temperature (Kelvin).

2.3.3. Deposition (Collision) Efficiency

Solution of equations (2.1) and (2.5) subject to the corresponding boundary conditions will yield the mass of particles entering the shell, the concentration of particles within

the spherical shell, and the mass of particles leaving the shell. Also, the flux of particles passing into the ideal sink will also be determined from that solution. The solution can then be used to determine the particle deposition efficiency, η, which is calculated as

$$\eta = \frac{I}{v_0 C_0 \frac{\pi d_p^2}{4}} \tag{2.10}$$

where I is the total particle deposition rate onto a collector, obtained by integrating the particle flux over the surface of the collector, υ_0 is the free stream (initial) water velocity [*Tufenkji and Elimelech*, 2004; *Yao et al.*, 1971]. This integration can be done readily with COMSOL.

2.3.4. Numerical Solution

A finite element based computational modeling and simulation software package, COMSOL Multiphysics® (COMSOL, Inc., Burlington, MA, USA), is chosen for simulating colloid deposition in this study due to its features that seemed to meet the above needs. This software is fast and reliable, allows creation of complex geometries, and the influences of boundary conditions can be assessed easily.

The simulations are performed, as in earlier studies [*Rajagopalan and Tien*, 1976; *Tufenkji and Elimelech*, 2004; *Yao et al.*, 1971], in an axisymmetric domain that provides three-dimensional results from two-dimensional simulations [*Nelson et al.*, 2007].

Triangular elements are used in the mesh system (Figure 2.2). The number of elements in the mesh system used in the simulations is determined by trial and error. The number of elements is increased until the results do not vary substantially. By default COMSOL generates mesh systems automatically. In our case with a sub-domain that

has a high aspect ratio, better results were obtained when the mesh system was created in part by manual specification of mesh generation parameters.

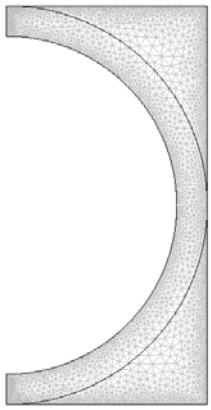

Figure 2.2. The mesh system used in this study

Once the mesh system was established the simulations were performed with colloid diameters varying from 0.05 to 2 μm, and a constant collector diameter of 0.6 mm as described in more detail in the next section.

2.4. SIMULATIONS: SETUP AND RESULTS

2.4.1. Colloid Deposition on a Grain Collector

In this section, the colloid deposition efficiency of a spherical solid grain (collector) is simulated numerically using COMSOL. The results are compared with three previous studies.

The boundary conditions for the solution of the Navier-Stokes equation are summarized in Table 2.1 and shown graphically in Figure 2.3. Flow direction and gravity are both opposite to the direction of the y-axis. The convection-diffusion equation is solved with the same boundary conditions as in *Yao et al.* [1971] except that, the colloid concentration at the fluid shell surface is set to be equal to the initial

concentration (Equation 2.8), while *Yao et al.* [1971] assumed the concentration to be equal to the initial concentration at an infinite distance from the collector surface.

Table 2.1. The boundary conditions used to solve the Navier-Stokes equation for a solid grain

Boundary	Condition
Inlet	v_0 = 9 x 10^{-6} m/s
Collector Surface	No-slip (v = 0 m/s)
Outlet	Atmospheric Pressure (0 Pa)
Sides, Fluid Shell	Symmetry

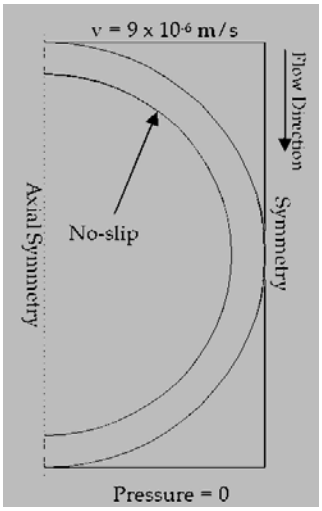

Figure 2.3. The boundary conditions for the Navier-Stokes Equation (solid grain)

In order to compare our results with the previous studies, the parameter values used in the simulations were adopted from the study of *Tufenkji and Elimelech* [2004] (Table 2.2). Simulations were performed for colloids with diameters of 0.05, 0.10, 0.50, 0.75, 1, 1.5, and 2 μm and a grain diameter of 0.6 mm. The most time-consuming step in our simulations was the trial and error generation of the mesh. Once the optimum mesh system was found, each simulation took an average of 37 seconds.

The simulation results are given in Figure. 2.4 together with the results of the three other studies. Similar to the other studies, colloid deposition efficiency is the greatest

for the 0.05 μm colloids than decreases with larger colloids diameter. When colloid diameters are on the order of 1 μm colloid deposition increases again (Figure 2.4).

Table 2.2. Variables used in the simulations [*Tufenkji and Elimelech*, 2004].

Variable		Value
d	Collector diameter	0.6 mm
v_0	Initial water velocity	9×10^{-6} m/s
T	Temperature	288 K
k	Boltzmann constant	$1.3806503\ 10^{-23}$ J/K
ε	Porosity	0.39
ρ_w	Density of water	1000 kg/m^3
ρ_p	Density of colloids	1050 kg/m^3
μ	Dynamic viscosity of water	0.001 Pa.s

The integration of the particle flux on the zero concentration boundary (Equation 2.6) reveals that the diffusion as well plays an important role in the increased collection efficiency because the ratio of the colloid efficiencies is not the same for the different colloid diameters.

A comparison of our simulated deposition efficiency with those of the other three studies is presented in Figure 2.4. It is observed that our results agree very well with the *Rajagopalan and Tien* [1976] results. The worst comparison is with the result of *Yao et al.* [1971], while an intermediate agreement is achieved with the results of *Tufenkji and Elimelech* [2004]. One reason our results are so different from the results of *Yao et al.* [1971] is that they did not incorporate the boundary effect of neighboring collectors into their solution. Another possible reason for the difference is that the efficiency calculations made by *Yao et al.* [1971] were based on the additivity assumption. While this assumption simplifies the solution, it could be problematic as noted by *Nelson and Ginn* [2005]. We do not yet know why our solution results disagree with those of *Tufenkji and Elimelech* [2004].

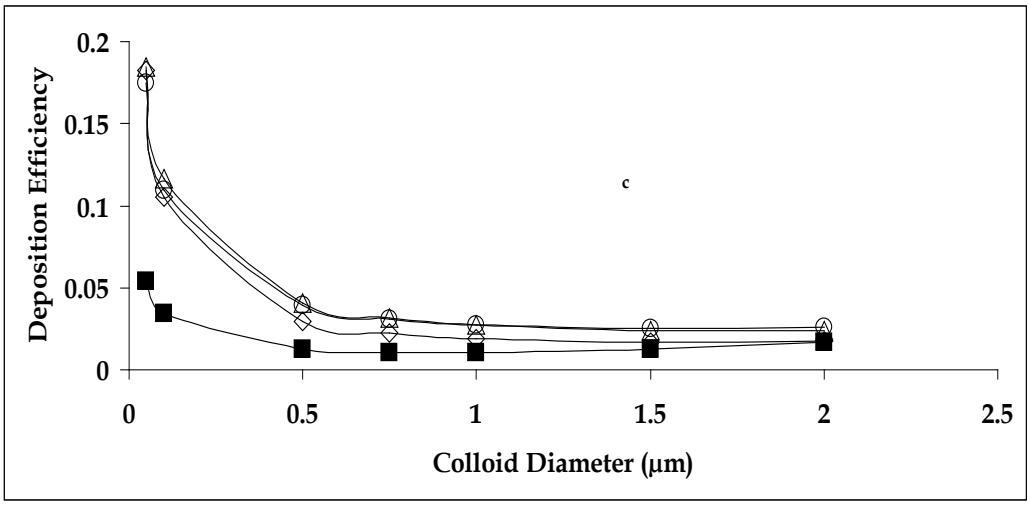

Figure 2.4. Deposition efficiency of a single collector vs. colloid size (diameter) (□)*Rajagopalan and Tien* [1976] (◊)*Tufenkji and Elimelech* [2004] (■)*Yao et al.* [1971] (○) Result of the current analysis

2.4.2. Colloid Deposition on an Air Bubble Collector

In this simulation of colloid deposition efficiency, the only change made was replacing the grain with an air bubble of the same size. For the numerical simulation this means that the no slip boundary becomes a slip boundary condition at the collector surface while the remaining parameter values and grid remain the same (Table 2.3 and Figure 2.5). The slip boundary has been used before for rising air bubbles in fluids by *Nguyen and Jameson* [2005] and *Shew and Pinton* [2006].

Table 2.3. The boundary conditions used to solve the Navier-Stokes equation for air bubble

Boundary	Condition
Inlet	$v_0 = 9 \times 10^{-6}$ m/s
Collector Surface	Slip ($v \neq 0$ m/s)
Outlet	Atmospheric Pressure (0 Pa)
Sides, Fluid Shell	Symmetry

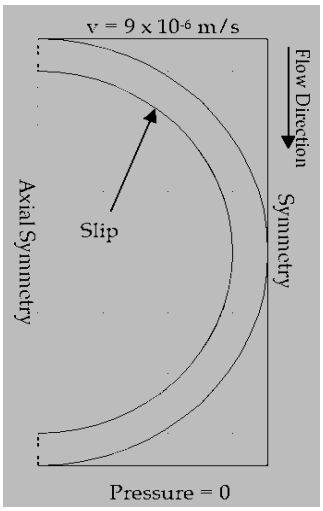

Figure 2.5. The boundary conditions for the Navier-Stokes Equation (air bubble)

The results of the simulation with the air bubble collector are compared to those for the solid particle in Figure 2.6. It is observed that the deposition efficiency of the air bubble is approximately twice that of the solid grain.

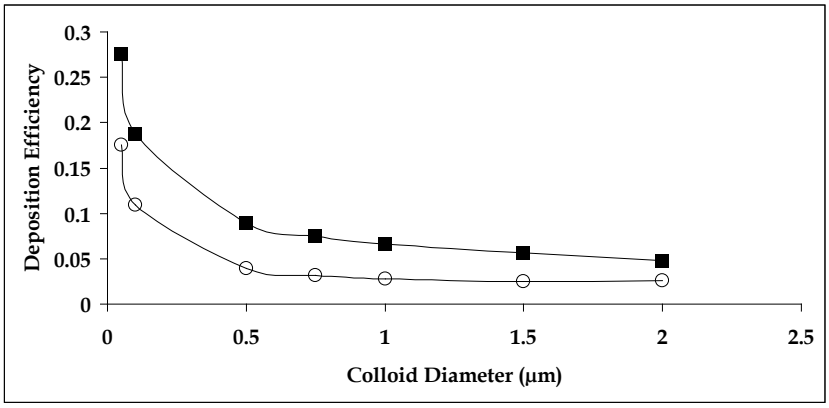

Figure 2.6. Deposition efficiency of the collectors vs. colloid size (diameter)
(■) Air Bubble (○) Solid Grain

The effects of the no-slip and slip boundaries on the water flow velocities are illustrated in Fig. 2.7. The water velocity around the air bubble is greater than the water velocity around the solid grain because under laminar flow conditions, the water

(and thus the colloid velocity) approaches zero near the grain surface.

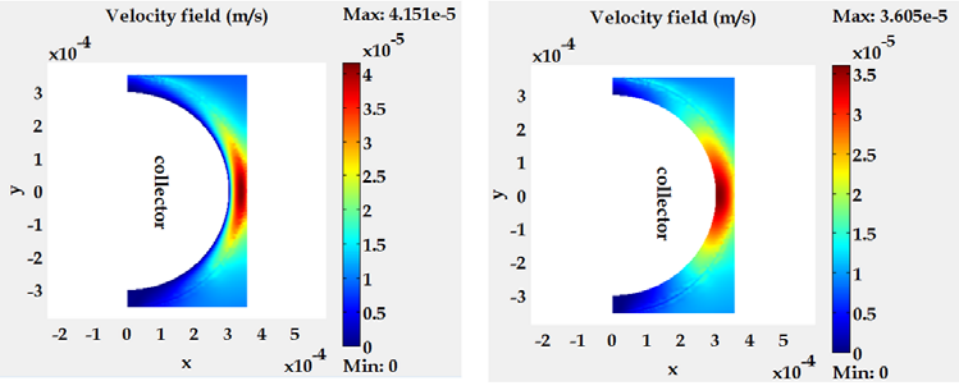

a) Solid Grain (No-Slip Boundary) b) Air Bubble (Slip Boundary)

Figure 2.7. Velocity fields around the collectors

The differences between the two cases are due to the relative fraction of colloids that come into the vicinity of the diffusion boundary. Regions of high velocity will transport a larger fraction of colloids in contrast to regions of low velocity. For the case of the bubble, the slip boundary results in high water velocity near the diffusion boundary and therefore a relatively high fraction of colloids will be transported in the vicinity of that boundary, resulting in higher concentration gradients at the diffusion boundary. For the case of the solid particle, the no-slip boundary results in a lower velocity near the diffusion boundary and therefore a relatively lower fraction of colloids will be transported in the vicinity of the diffusion boundary, resulting in lower concentration gradients at that boundary. That the difference between the two cases decreases as the particle size increases can be explained by fact that as the colloid diffusion decreases (with increasing diameter) the differences in transport across the diffusion boundary will also decrease. As the diffusion becomes vanishingly small, the colloid concentrations at the diffusion boundary will be identical for the two cases, exactly equal to the initial concentration, C_0.

While various surface forces (capillary, DLVO, electrostratic, etc.) were not considered in our analysis, the differences in flow velocity near the collector surface between the solid collector and the air bubble are expected to have significant influence on the predicted efficiency of colloid deposition when such forces are incorporated into the governing transport equations [*Elimelech et al.,* 1995; *Tien and Ramarao,* 2007].

2.5. CONCLUSIONS

The re-examination of the colloid filtration theory revealed that it is crucial to consider the effect of surrounding solid grains on the flow field in order to gain more realistic results.

The application of the colloid filtration theory on the air bubble showed that more colloids collided with the air bubble than with the solid grain due to high pore water velocity around its surface. The pore water velocity and the disturbances in the flow field have a substantial effect on the deposition and transport paths of the colloids. Nevertheless, in order to thoroughly examine the effect of pore water velocity on the dominant deposition mechanism, the simulations should be done with various initial water velocities. To better model an unsaturated porous medium, simulations with assemblages of collectors need to be performed.

2.6. FUTURE WORK

Our simulations of the colloid deposition in unsaturated porous media need to be extended to take domains composed of assemblages of collectors into account. We are interested to study the variables/parameters that will affect the colloid deposition.

It is planned to construct a model porous medium consisting of solid grains and air bubbles in two dimensions and three dimensions. This is expected to provide more insight into the colloid deposition for unsaturated conditions.

REFERENCES

Auset, M., and A. A. Keller (2004), Pore-scale processes that control dispersion of colloids in saturated porous media, Water Resour. Res., 40(3), -, doi: Artn W03503 Doi 10.1029/2003wr002800.

Corapcioglu, M. Y., and H. Choi (1996), Modeling colloid transport in unsaturated porous media and validation with laboratory column data, Water Resour. Res., 32(12), 3437-3449.

Crist, J. T., Y. Zevi, J. F. McCarthy, J. A. Throop, and T. S. Steenhuis (2005), Transport and retention mechanisms of colloids in partially saturated porous media, Vadose Zone J., 4(1), 184-195.

DeNovio, N. M., J. E. Saiers, and J. N. Ryan (2004), Colloid movement in unsaturated porous media: Recent advances and future directions, Vadose Zone J., 3(2), 338-351.

Elimelech, M. (1994), Particle Deposition on Ideal Collectors from Dilute Flowing Suspensions - Mathematical Formulation, Numerical-Solution, and Simulations, Separations Technology, 4(4), 186-212.

Elimelech, M., J. Gregory, X. Jia, and R. A. Williams (1995), Particle Deposition and Aggregation Measurement, Modelling and Simulation, Butterworth-Heinemann, Oxford.

Happel, J. (1958), Viscous Flow in Multiparticle Systems - Slow Motion of Fluids Relative to Beds of Spherical Particles, AlChE J., 4(2), 197-201.

Keller, A. A., and S. Sirivithayapakorn (2004), Transport of colloids in unsaturated porous media: Explaining large-scale behavior based on pore-scale mechanisms, Water Resour. Res., 40(12), -, doi: Artn W12403

Doi 10.1029/2004wr003315.

Keller, A. A., and M. Auset (2007), A review of visualization techniques of biocolloid

transport processes at the pore scale under saturated and unsaturated conditions, Adv Water Resour, 30(6-7), 1392-1407, doi: DOI 10.1016/j.advwatres.2006.05.013.

Lenhart, J. J., and J. E. Saiers (2002), Transport of silica colloids through unsaturated porous media: Experimental results and model comparisons, Environ. Sci. Technol., 36(4), 769-777, doi: Doi 10.1021/Es0109949.

Nelson, K. E., and T. R. Ginn (2005), Colloid filtration theory and the Happel sphere-in-cell model revisited with direct numerical simulation of colloids, Langmuir, 21(6), 2173-2184, doi: Doi 10.1021/La048404i.

Nelson, K. E., A. Massoudieh, and T. R. Ginn (2007), E. coli fate and transport in the Happel sphere-in-cell model, Adv Water Resour, 30(6-7), 1492-1504, doi: 10.1016/j.advwatres.2006.05.027.

Nguyen, A. V., and G. J. Jameson (2005), Sliding of fine particles on the slip surface of rising gas bubbles: Resistance of liquid shear flows, Int. J. Multiphase Flow, 31(4), 492-513, doi: 10.1016/j.ijmultiphaseflow.2005.01.005.

Rajagopalan, R., and C. Tien (1976), Trajectory Analysis of Deep-Bed Filtration with Sphere-in-Cell Porous-Media Model, AlChE J., 22(3), 523-533.

Ryan, J. N., and M. Elimelech (1996), Colloid mobilization and transport in groundwater, Colloids Surf., A, 107, 1-56.

Shew, W. L., and J.-F. Pinton (2006), Viscoelastic effects on the dynamics of a rising bubble, Journal of Statistical Mechanics: Theory and Experiment, 2006(01), P01009.

Spielman, L. A. (1977), Particle Capture from Low-Speed Laminar Flows, Annual Review of Fluid Mechanics, 9, 297-319.

Tien, C., and B. V. Ramarao (2007), Granular Filtration of Aerosols and Hydrosols, 2nd ed., Butterworth-Heinemann, Great Britain.

Tufenkji, N., and M. Elimelech (2004), Correlation equation for predicting single-collector efficiency in physicochemical filtration in saturated porous media, Environ.

Sci. Technol., 38(2), 529-536, doi: Doi 10.1021/Es034049r.

Yao, K. M., M. M. Habibian, and C. R. Omelia (1971), Water and Waste Water Filtration - Concepts and Applications, Environ. Sci. Technol., 5(11), 1105-1112.

Zevi, Y., A. Dathe, J. F. Mccarthy, B. K. Richards, and T. S. Steenhuis (2005), Distribution of colloid particles onto interfaces in partially saturated sand, Environ. Sci. Technol., 39(18), 7055-7064, doi: 10.1021/Es048595b.

CHAPTER 3
MICROFLUIDICS NEAR ROUGH SURFACES: ESTIMATES OF LOW VELOCITY AREAS ENHANCING COLLOID RETENTION

3.1. ABSTRACT

Theories describing colloid behavior in porous media assume, in most cases, that colloids interact with smooth grain surfaces. Experimental observations in natural sands deviate from these theoretical predictions, with the discrepancies recently attributed to grain surface physical and electrical heterogeneities. This study explores the effect of surface roughness on possible colloid retention by comparing pathways created by micron-scale surface asperities with those around smooth grains by solving the Stokes equation using the finite element method. Graphically, the results show that streamlines form vorticities around the rough grains at locations where they do not exist around smooth grain surfaces. Quantitatively the water has a lower velocity around the rough grains than for the smooth grain. Presence of lower velocities and greater vorticity can enhance colloid deposition. Thus, rough grains could have more colloid retention than smooth grains under otherwise similar conditions.

3.2. INTRODUCTION

Colloidal transport in the subsurface has gained attention over the past few decades as enhanced transport of contaminants in groundwater, permeability of oil and gas reservoirs, and on-site remediation strategies have become topics of concern in various fields of environmental science and engineering. Groundwater protection is of specific concern, because it has been shown that colloids facilitate the transport of otherwise immobile contaminants by carrying them much further and faster than would be predicted with traditional solute transport models [*McCarthy and McKay*, 2004; *Ryan*

and Elimelech, 1996].

Colloid transport in porous media has conventionally been modeled by colloid filtration theory (CFT), which solves the convection-diffusion equation using a velocity field for a perfectly smooth and homogeneous isolated spherical grain. Colloid deposition from the suspension occurs when colloids are transferred onto the grain surface by interception, gravitational settling, and Brownian diffusion in the absence of repulsive energy barriers (i.e. under favorable attachment conditions) [*Yao et al.*, 1971]. However, significant colloid retention has also been observed under conditions deemed to be unfavorable for attachment [*Bradford and Torkzaban*, 2008; *Johnson et al.*, 2007a]. Potential mechanisms of colloid deposition in the presence of an energy barrier in saturated and unsaturated soils include: i) retention at interfaces (e.g., solid-water and air-water) [*Bradford and Torkzaban*, 2008; *Wan and Wilson*, 1994]; ii) retention at the intersects of multiple interfaces, which could include wedging [*Johnson et al.*, 2007b; *Li et al.*, 2006], straining [*Bradford et al.*, 2006; *Cushing and Lawler*, 1998], and retention at air-water-solid interfaces [*Crist et al.*, 2004; *Wan and Wilson*, 1994; *Zevi et al.*, 2005]; iii) retention in immobile water zones [*Gao et al.*, 2006; *Torkzaban et al.*, 2008]; iv) retention via association with secondary energy minima in zones of low fluid drag [*Hahn and O'Melia*, 2004]. In unsaturated media, colloids may additionally be retained by bridging [*Crist et al.*, 2005] and film straining under capillary and friction forces, and/or due to meniscus deformation [*Gao et al.*, 2008; *Morales et al.*, 2009; *Wan and Tokunaga*, 1997].

In order to explain the above listed retention mechanisms, various forces experienced by colloids have been considered including: colloidal, capillary, hydrodynamic, Brownian, and gravitational forces [*Bradford et al.*, 2007; *Johnson et al.*, 2007b; *Ma*

et al., 2009; *Torkzaban et al.*, 2007]. The forces between colloid-interface (e.g. Solid-Water and Air-Water-Solid interfaces), and colloid-colloid are generally determined with Derjaguin-Landau-Verwey-Overbeek (DLVO) theory, which assumes that interfaces are perfectly smooth and homogeneous and excludes any hydrodynamic component present in the system being studied [*Adamczyk et al.*, 1983; *Elimelech et al.*, 1995; *Tien and Ramarao*, 2007].

A number of studies, including those by *Elimelech and Omelia* [1990], *McBride* [1997], *Bradford and Torkzaban* [2008], and *Kemps and Bhattacharjee* [2009], state that while models in accordance with CFT and DLVO theories give reasonable predictions for smooth and homogeneous grain surfaces, these classic theories fail to predict colloid deposition on more realistic and heterogeneous media. *Tobiason* [1989] studied the effect of changing solution chemistry on the deposition of non-Brownian colloids, and reported a significant discrepancy between modeled and experimentally observed results in the presence of a repulsive double layer. The report consequently attributed the discrepancy to surface roughness. *Elimelech and Omelia* [1990] experimentally observed that the amount of colloids deposited at porous medium retention sites was sensitive to solution chemistry (e.g., electrolyte concentration and counter-ion type), but not to the extent predicted by DLVO theory. *Shellenberger and Logan* [2002] found that under saturated conditions, the amount of inorganic colloids deposited on rough surfaces was 30-50% greater than for smooth surfaces. In another experimental study, *Morales et al.* [2009] showed that significantly more colloids were retained under both saturated and unsaturated conditions by sand grains with rough surfaces than by grains with smoothed surfaces.

Two studies [*Hoek et al.*, 2003; *Suresh and Walz*, 1996] used the change in total

interaction energy between colloid and grain surface to explain the increased retention with increasing grain roughness, while discounting possible hydrodynamic effects. *Suresh and Walz* [1996] explained that the observed increase in retention for rough grains was caused by an interaction energy decrease in primary maxima and increase in secondary minima of rough vs. smooth grains. These predictions were subsequently confirmed by *Hoek et al.* [2003] who investigated the effect of membrane surface roughness on colloid-membrane interaction energies (i.e., total DLVO forces) with atomic force microscopy and reported that the magnitude of repulsive forces was decreased by the membrane's asperities. Another study by *Saiers and Ryan* [2005] included hydrodynamic effects in the colloid filtration (CFT) theory to predict greater colloid deposition for rough surfaces by attributing the observed increase in colloid collision efficiency to surface roughness. This is supported in part by visual observations of pore-scale colloid movement in our laboratory, notably colloids circle in vorticities caused by non-standard flow patterns induced by rough and irregularly shaped soil grains (Movie I – Please see Appendix). There are very few if any simulations that have been able to duplicate these circling of colloids for laminar flow. Simulations that have been performed for particle deposition are for turbulent flow [*Grass et al.*, 1991; *Ounis et al.*, 1991; *Morrison et al.*, 1992; *Li and Ahmadi*, 1993]. Under turbulent flow conditions vortexes are expected [*Abuzeid et al.*, 1991; *Fan and Ahmadi*, 1995] but the existence of vorticity for laminar flow is not well researched. It is our intent to simulate flow lines that could be responsible for colloid retention.

Some of the researchers simulating colloid transport have customized computer codes. *Johnson et al.* [2007b] developed a three-dimensional particle tracing model to estimate colloid deposition in porous media in the presence of energy barrier. *Li et al.* [2010] examined the importance of low flow zones and flow vorticities by using

Lattice-Boltzmann simulations. *Shi et al.* [2010] used the Lattice-Boltzmann technique to show that for a moving contact line in a microchannel there is counter flow along the walls under viscous flow conditions. Experimental studies show that colloids moved opposite the flow direction. Other studies have used the finite element analysis software COMSOL in colloid transport studies [*Cakmak et al.*, 2008; *Kemps and Bhattacharjee*, 2009; *Torkzaban et al.*, 2007]. In [*Cakmak et al.*, 2008] the COMSOL Multiphysics (COMSOL, Inc., Burlington, MA, USA), finite element solution was compared with the results calculated by collision efficiency equations derived with semi-analytical and semi-empirical solutions of *Yao et al.* [1971], *Rajagopalan and Tien* [1976], and *Tufenkji and Elimelech* [2004]. In this simulation a spherical grain was enclosed and the surrounding fluid sphere in a cube. The fluid sphere was continuity boundary condition with the sides of the cube parallel to the general flow direction had a symmetry boundary where tangential stress is zero and no flow normal to the boundary. At the sides of the cube perpendicular to the flow direction a pressure difference was defined to create fluid flow. We simulated the deposition of colloids with diameters ranging from 0.05 to 1 μm on a grain with the diameter of 0.6 mm. The simulated deposition rates agreed very well with that of *Rajagopalan and Tien* [1976] and reasonably with that of *Tufenkji and Elimelech* [2004] (Figure 3.3). In general we found that the COMSOL software was fast and reliable. Another advantage of the COMSOL software is the relatively easy creation and meshing of complex geometries needed to simulate rough grains and the influences of boundary conditions can be assessed. For these reasons the COMSOL software was selected in order to be able to represent the rough grain surfaces realistically.

Experimental evidence on increased retention of colloids for rough grains in a porous medium highlight the need to incorporate, realistic flow patterns into colloid transport

models. This study, therefore, explores the effect of grain-surface heterogeneity on fluid flow near the grain surface with computational simulations using COMSOL Multiphysics. Three levels of surface roughness are used (perfectly smooth, smoothed, and naturally rough) to determine the role of microfluidics in the discrepancy of colloid retention between experimental observations with heterogeneous medium grains and theoretical calculations that assume spherical collectors. Because colloid retention requires that colloids come close proximity to the grain surface, it is critical to know more about one of the least understood external forces, namely hydrodynamics for rough surfaces under viscous flow conditions. Up to now nearly all simulations with colloid deposition have been carried for various flow around perfectly smooth surface or turbulent flow with both rough and smooth surfaces.

3.3. MATERIALS AND METHODS

3.3.1. Simulation Methodology

Flow patterns around the grain surfaces were calculated with the COMSOL' built in steady-state incompressible Stokes equations:

$$\nabla p = \mu \nabla^2 v \tag{3.1}$$

$$\nabla \cdot v = 0 \tag{3.2}$$

where p is the fluid pressure (Pa), v is the velocity of the water (m/s), μ is the dynamic viscosity of the water (0.001 Pa·s). Equations 3.1 and 3.2 were solved based on finite element method using COMSOL Multiphysics® v3.5a (COMSOL, Inc., Burlington, MA, USA). Care was taken that in all cases Reynolds number was much lower than unity in order to establish creeping flow conditions in the simulations.

Two different sets of simulations were carried out to show the effect of grain roughness on flow pattern. Simulation set 1 compares 3-dimensional fluid flow paths over two individual sand grains with two different degrees of surface roughness (smoothed and naturally rough) to determine the effect of surface heterogeneity on fluid flow at the pore scale. Simulation set 2 compares 3-dimensional fluid flow simulations of small sections of three grain surfaces with different degrees of roughness (smooth, smoothed, and naturally rough) to observe the detailed effects of surface asperities on fluid streamlines at close proximity to the grain surface. The necessary grain geometries for both sets of simulations were built using COMSOL Script v.1.2 with the topographic data obtained by optical interferometry of real grain surfaces (Figures A1 and A2 in Appendix).

Set 1 simulations: A perfectly smooth single spherical grain was generated with the diameter of 0.6 mm (Figure 3.1a) using COMSOL's Draw Mode. A 3-D single spherical sand grain with a naturally rough surface (Figure 3.1b) was generated using COMSOL Script. Since naturally rough sand grains do not show a uniform asperity size and distribution over the surface, thus a random asperity size and distribution was generated over the 3-D surface (with a diameter of 0.6 mm) within a peak to valley range of 10-40 μm.

Boundary condition were set at the grain surface and the and the sites of the fluid cube surrounding the sand grains [*Cakmak et al.*, 2008; *Tien and Ramarao,* 2007]. The surfaces of the grains were taken as no-slip boundary condition (i.e., water velocity on the grain surface is zero) [*Tien and Ramarao,* 2007]. The sides of the cube, with a length of 0.7117 mm, parallel to main direction of flow was a symmetry boundary condition, with no flow normal to the boundary and no tangential stress at the

boundary. The top of the cube was set as inlet velocity boundary 4×10^{-4} m/s and the bottom of the cube was specified as outlet boundary with zero pressure. The flow direction was from top to bottom of the domain. Note that these boundary conditions are slightly different than that of *Cakmak et al.* [2008] since the solution with the continuity boundary condition in a sphere around the grain did not converge in 3D due to difficulties while generating the correct mesh. Therefore, in order to validate the COMSOL's results with the revised boundary conditions, the collision efficiencies were recalculated for 5 colloid sizes with the same procedure by *Cakmak et al.* [2008] with COMSOL. The results were compared with results in the *Yao et al.* [1971], *Rajagopalan and Tien* [1976], and *Tufenkji and Elimelech* [2004] papers (Figure 3.3).

In the axisymetrical simulations for the recalculation of collision efficiencies a mesh system consisting of 30,000 triangular elements was used. For the set 1 simulations of this study the solution converged with nearly 140,000 and 180,000 micron-sized triangular elements distributed throughout the 3-dimensional domain (perfectly smooth and naturally rough, respectively) (Figure 3.1c and 3.1d). Convergence is internally controlled by COMSOL software.

Set 2 simulations: In order to obtain a detailed view of how micron-sized surface asperities affect fluid flow pattern near grain surfaces, a detailed flow pattern around the 3-D grain surface domain was reduced from whole grains to 0.01 mm^2 areas with fluid field thicknesses of 0.06 mm. Perfectly smooth, smoothed, and naturally rough grain surfaces were generated using COMSOL Script v1.2 and COMSOL's draw mode. Here, the software defined perfectly smooth grain surfaces with a mean peak-to-valley height of 0 μm (Figure 3.2a), smoothed grain surfaces with a mean peak-to-valley height of 20 μm (Figure 3.2b), naturally rough grain surfaces with a mean peak-

to-valley height distributions ranging from 10-40 μm (Figure 3.2c). Two flow directions (one orthogonal and one parallel to the grain) were applied to each of the three surfaces at specified pressure differences of 1×10^{-4} Pa between inlet (left/top) and outlet (right/bottom) of the domain, rendering an average approach velocity of 2×10^{-6} m/s.

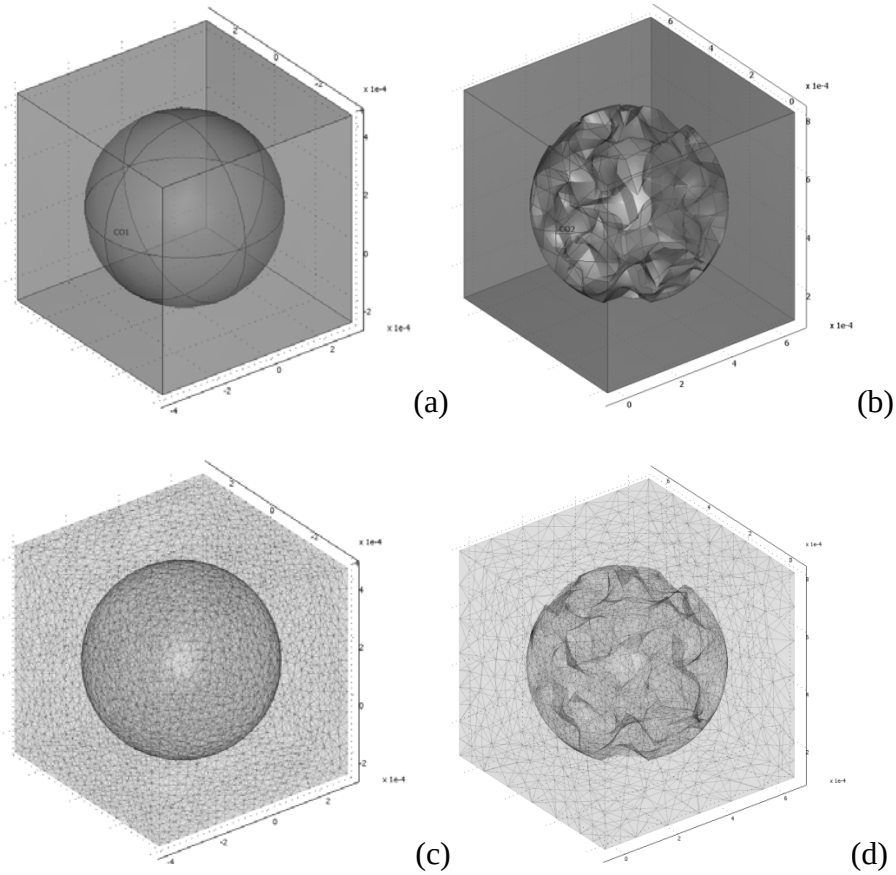

Figure 3.1. 3-D geometries of: (a) a perfectly smooth single spherical grain, (b) a single spherical sand grain with a naturally rough surface, (c) and (d) their meshed geometries with nearly 130,000 triangular mesh elements (Units of the axes are meters).

The grain surface was specified as no-slip boundary. The remaining sites of the domain were set as symmetry boundaries, where the tangential component of total

stress and normal component of velocity are set to zero. In the set 2 simulations the mesh system was initially generated automatically by COMSOL producing nearly 10,000 triangular elements and the number of the meshes was, then, gradually increased to obtain convergence and reliable results (at the end nearly 60,000 micron-sized triangular distributed throughout the domain).

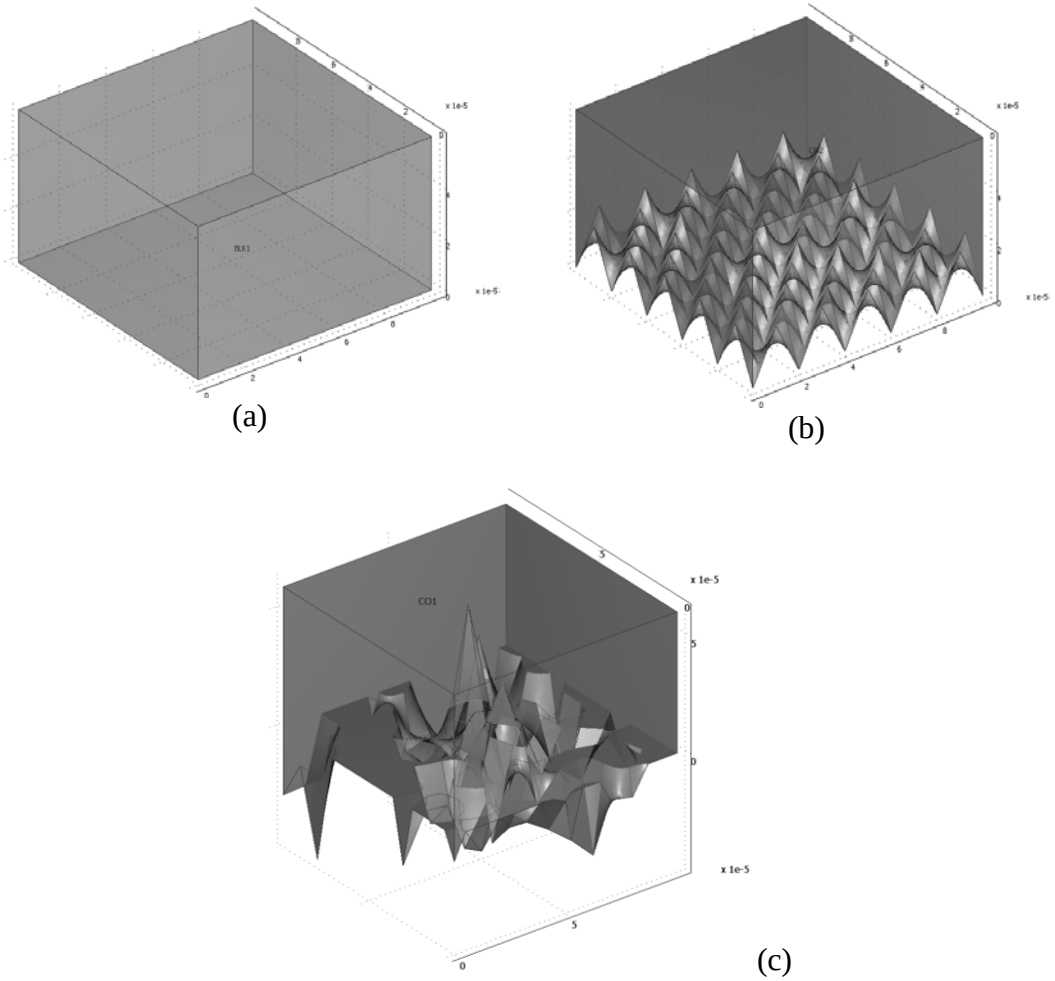

Figure 3.2. Sections of 0.01 mm^2 for: (a) a perfectly smooth sand grain surface, (b) a smoothed sand grain surface, and (c) a naturally rough sand grain surface Units of the axes are meters).

3.4. RESULTS

Set 1 Simulations: The collision efficiencies for the four colloid sizes is compared with the experimental and numerical results of *Yao et al.* [1971], *Rajagopalan and Tien* [1976], and *Tufenkji and Elimelech* [2004] in Figure 3.3. There is clear difference in collision efficiency depending on the boundary conditions. The original *Cakmak et al.* [2008] fit that of *Rajagopalan and Tien* [1976], and *Tufenkji and Elimelech* [2004] best because they all three used Happel's model with a fluid sphere around the grain. Our recalculated colloid efficiencies without Happel's model underestimate the experimental results of *Yao et al.* [1971] slightly and an overall good fit was obtained.

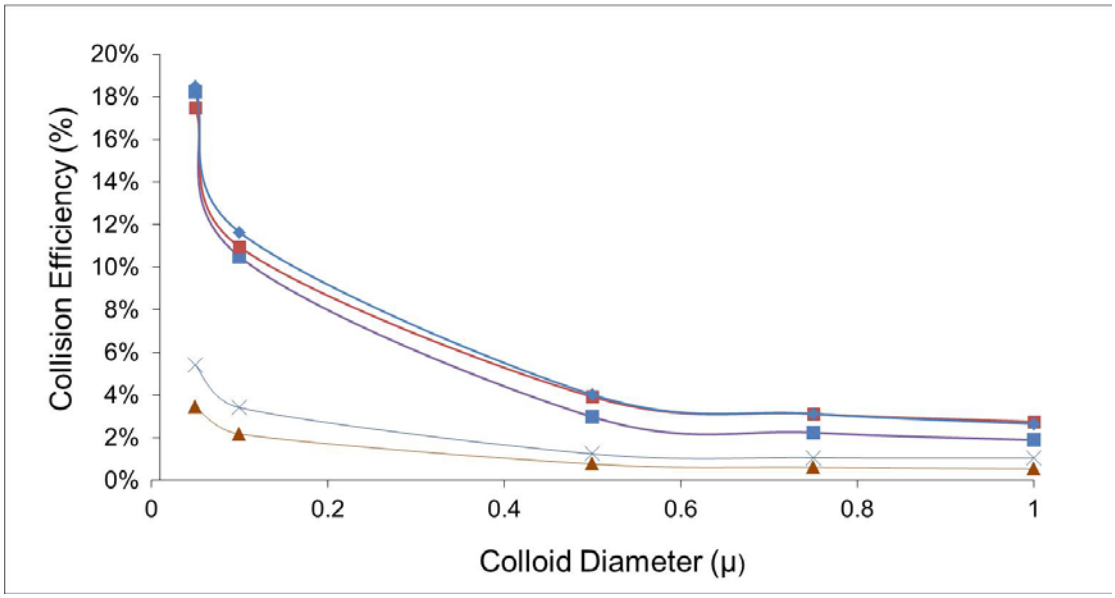

Figure 3.3. Collision efficiency of a single soil grain (■) *Tufenkji and Elimelech* [2004], (■) COMSOL's solution of *Cakmak et al.* [2008] with symmetry boundary condition, (♦) *Rajagopalan and Tien* [1976], (×) *Yao et al.* [1971], (▲)COMSOL's solution of *Cakmak et al.* [2008] for isolated-sphere model.

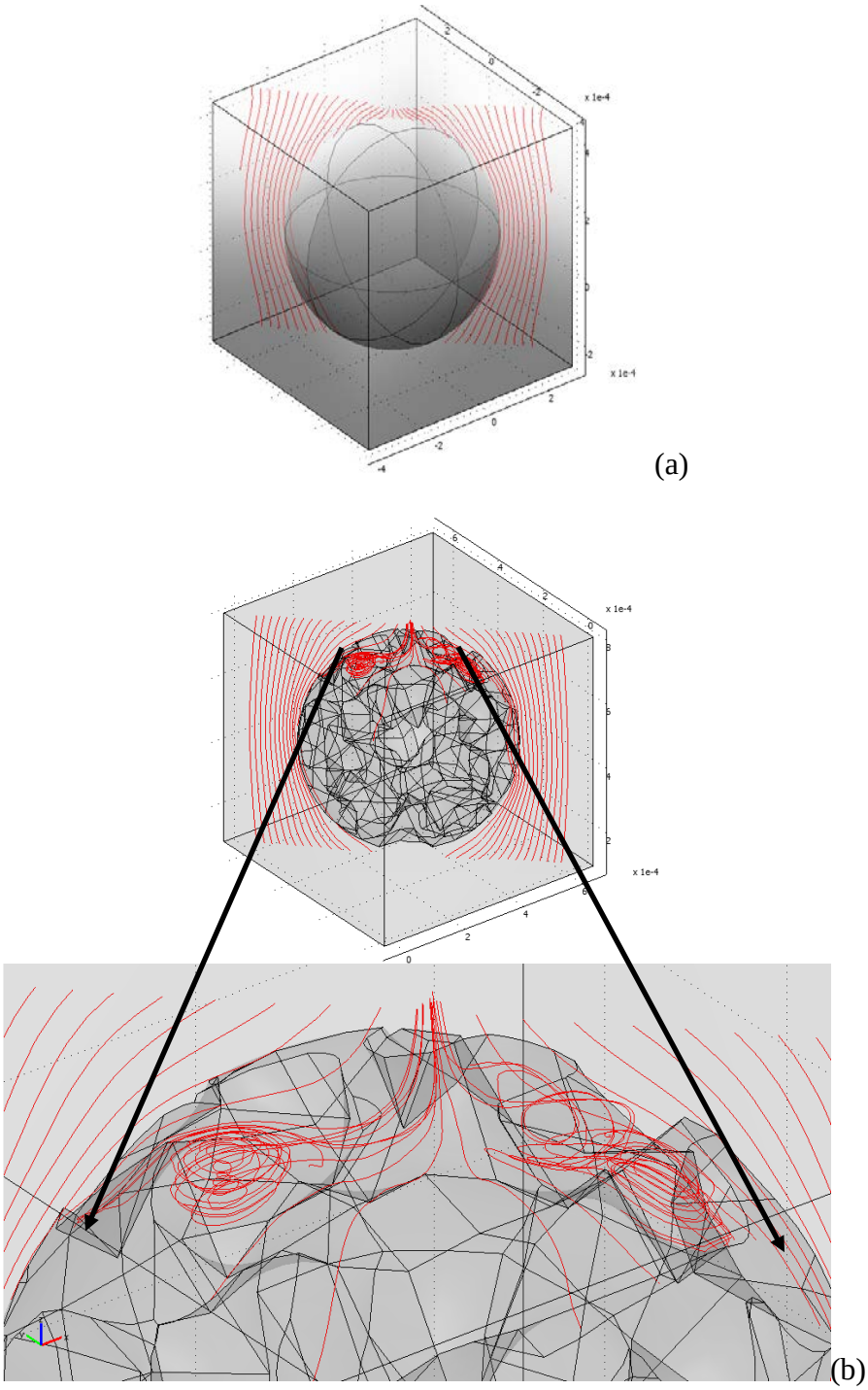

(a)

(b)

Figure 3.4. Fluid flow lines over (a) a perfectly smooth, and (b) a naturally rough sand grains placed in cubical domains (Units of the axes are meters).

Flow field results of the Set 1 3D simulations for a perfectly smooth and a naturally rough spherical grain in a cubic matrix are illustrated in Figures 3.4a and 3.4b, respectively. To simplify the density of data output, only selected stream lines (red lines) are included in each figure to illustrate the general flow pattern trends. For the rough grain simulations, distortion of the streamlines indicates that the asperities of the non-slip boundary significantly affect the fluid flow around the grain (Figure 3.4b). Although the streamlines farthest away from the grain are very similar for both surfaces, the flow lines close to the rough grain were much longer and tortuous than those enveloping the perfectly smooth grain (Figure 3.4b).

Figure 3.5 depicts the fluid velocity field around perfectly smooth and the naturally rough spherical grains within two dimensional cross-sections at the middle points of the axes (Figures 3.5a and 3.5b, respectively) in order to avoid intricacy in the figure. The dark blue regions indicate very low/zero flow velocity field whereas fluid velocity gets its highest rate in red regions. The distortion of flow paths by grain surface asperities indicates that surface roughness is a critical factor that impacts the hydrodynamics near the grain surface, which could significantly affect colloid deposition mechanics.

To indicate the higher possibility of colloid retention on the naturally rough grain than on the perfectly smooth grain the area fractions of the fluid velocity in Simulation set 1 is illustrated in Figure 3.6. It is clearly seen that the fraction of the areas having slower velocities are higher in the simulation of naturally rough grain than in the simulation of perfectly smooth grain. Colloids could be more retained in areas with slower velocities due to the possible formations of stagnant/low flow regions.

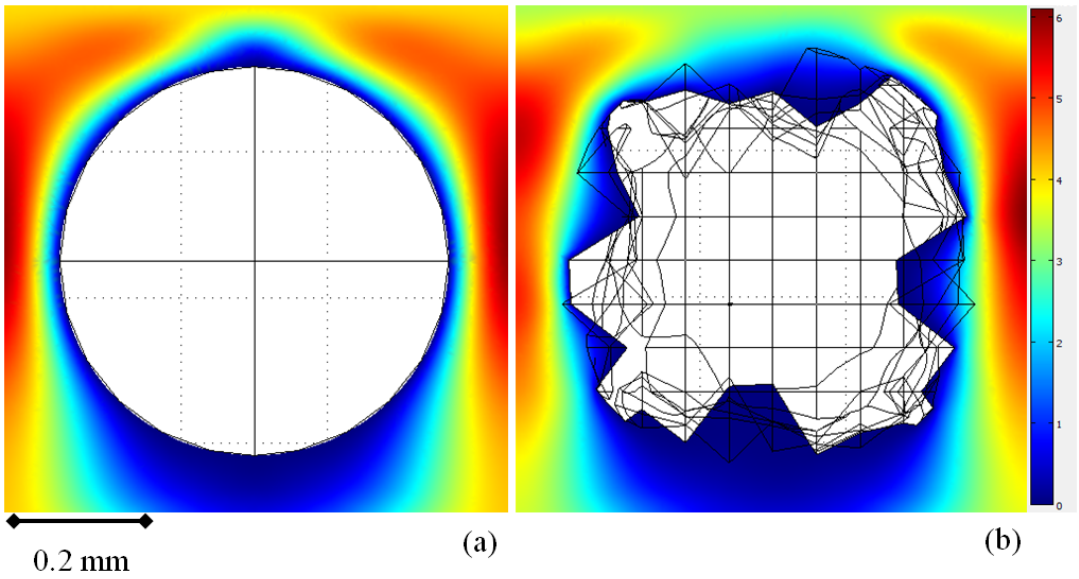

Figure 3.5. The fluid velocity fields within two dimensional cross-sections of the simulations of fluid flow over (a) the perfectly smooth and (b) the naturally rough spherical grains. Flow direction is from up to down (Ranging from 0 to 6×10^{-4} m/s).

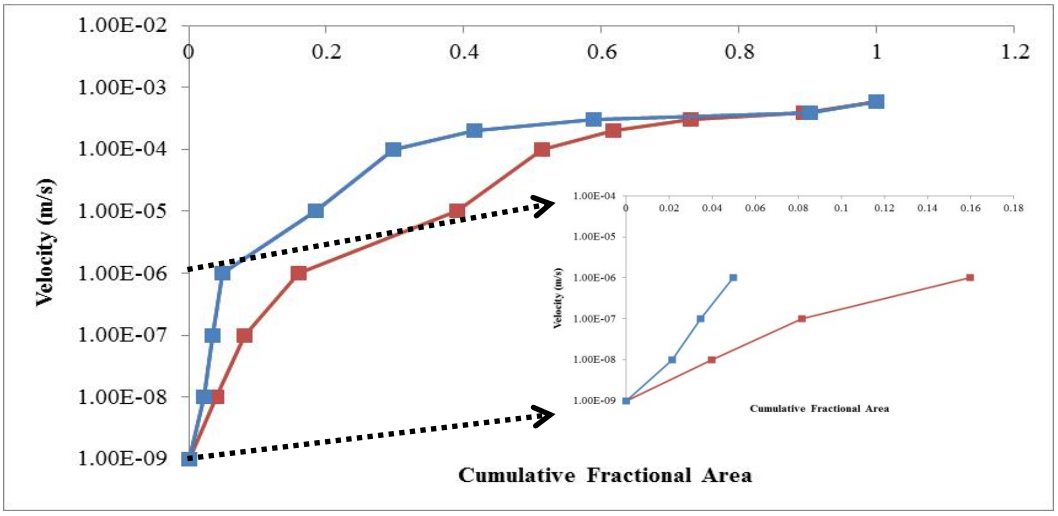

Figure 3.6. The area fraction of the fluid velocity depicted in Figure 3.5 (■) perfectly smooth grain (■) naturally rough grain.

In order to obtain a more detailed assessment of this effect, Set 2 simulations were generated to assess in greater detail the distortion of fluid flow near grain surfaces of various degrees of roughness.

Set 2 Simulations: In Figure 3.7, selected streamlines (red arrows) for a perfectly smooth grain surface illustrate parallel flow direction (Figure 3.7a) with exceptional linear uniformity. Figure 3.7b illustrates the flow orthogonal to the grain surface, which intercepts the grain and consequently moves parallel to the grain. The flow patterns simulated for either flow direction are uniform and do not deviate from the most direct path toward the exit point of the domain. These simplified flow paths conform to those proposed for ideal colloid filtration models [*Tien and Ramarao*, 2007].

Figure 3.8 illustrates the streamlines of flow over the smoothed grain surface (Movie II - Appendix). For flow in the direction parallel to the grain surface, it is evident that the asperities mildly disturb the flow in the valleys of the surface topography (Figure 3.8a) by generating small vorticities, but generally resemble the streamlines for the perfectly smooth grain surface (Figure 3.7a) at distances greater than 20μm away from the mean surface.

For flow orthogonal to the grain surface (Figure 3.8b), the flow pattern away from the grain surface is more severely affected by the surface asperities, creating a tortuous path between the points where the flow intercepts the grain until it reaches the edge of the domain. This lengthened pathway is in agreement with the whole-grain simulations obtained from Simulation set 1 (Figure 3.4b).

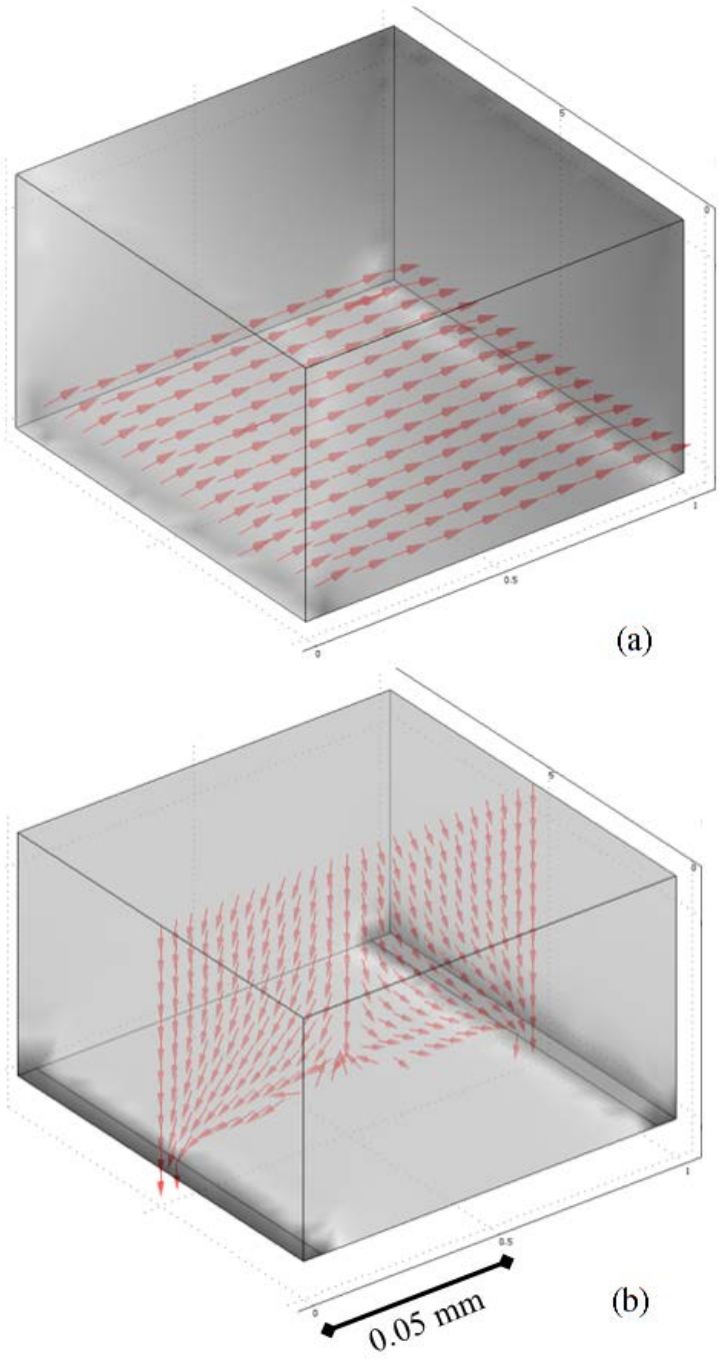

Figure 3.7. The surface (0.01 mm^2) of the perfectly smooth grain. The normalized velocity field is shown by arrows as fluid flows (a) tangential and (b) orthogonal to the surface.

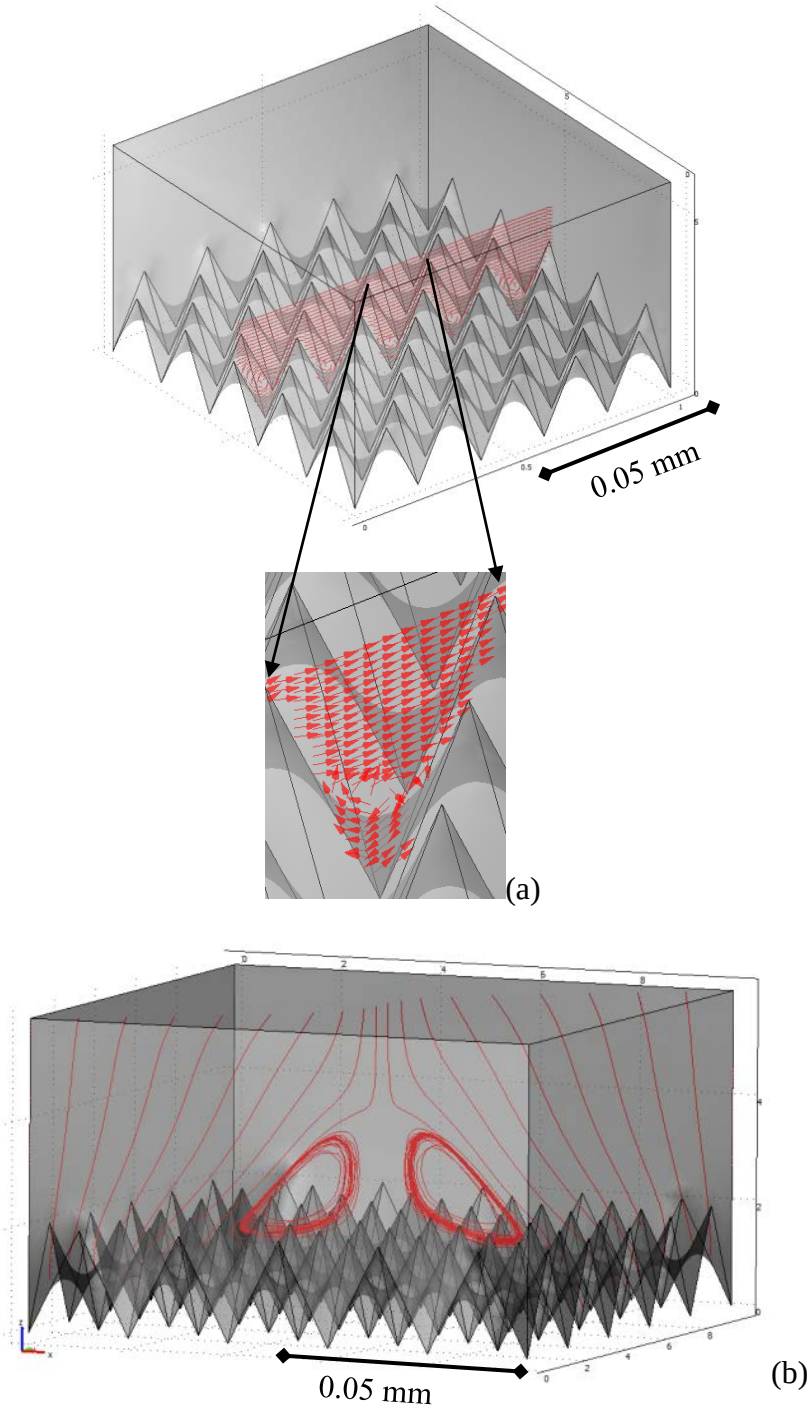

Figure 3.8. The surface (0.01 mm^2) of the smoothed grain with uniform asperity distribution and size (20 μm). (a) The normalized velocity field is shown by the arrows as fluid flows tangential to the surface and (b) the velocity field is shown by the red lines as fluid flows orthogonal to the surface.

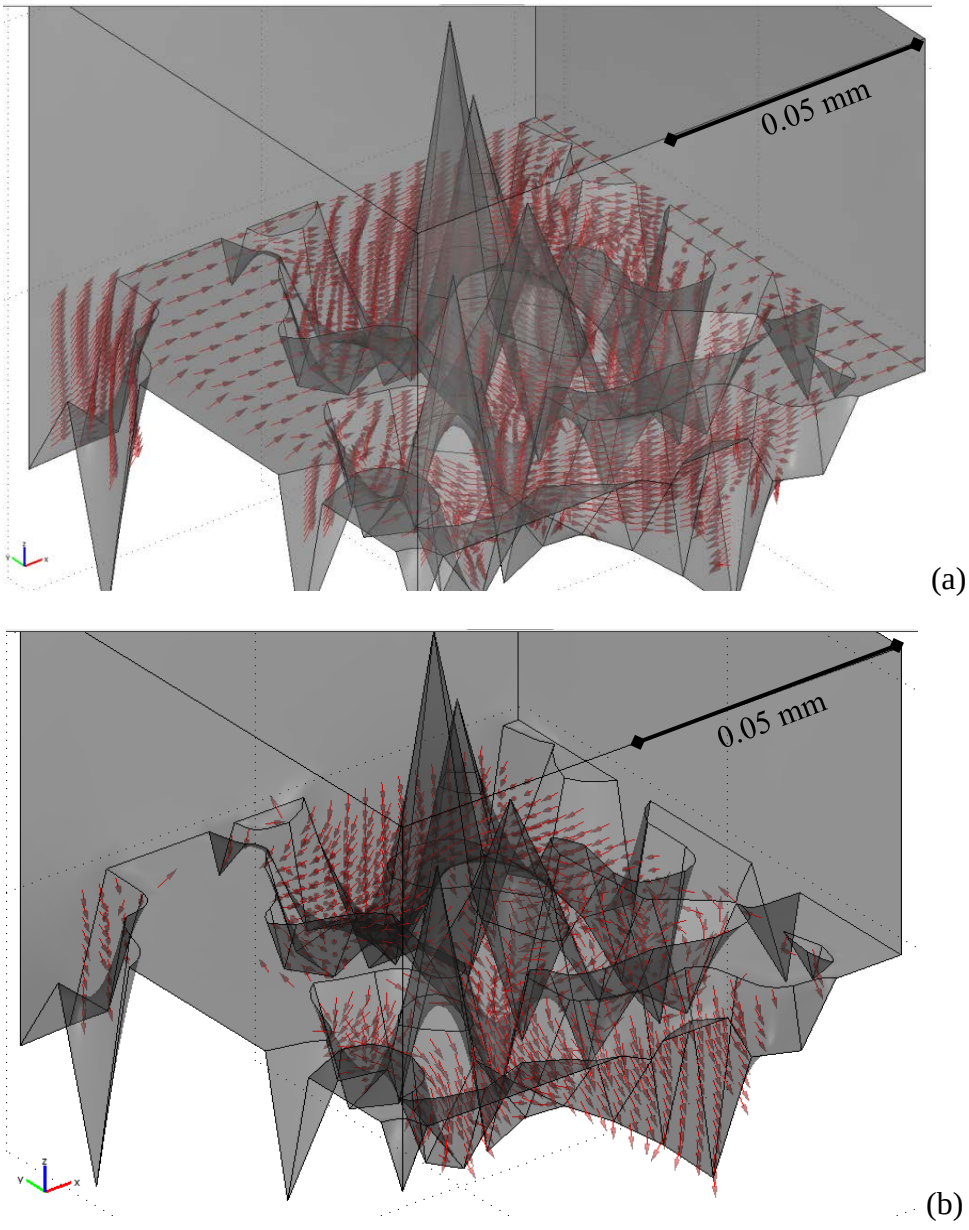

Figure 3.9. A naturally rough grain surface (0.01 mm^2) with non-uniform asperity distribution and size (10-40 μm) (a) The normalized velocity field is shown by the arrows as fluid flows tangential to the surface, (b) The normalized velocity field is shown by the arrows as fluid flows orthogonal to the surface.

Streamlines for parallel and orthogonal flow over the naturally rough grain surface are illustrated in Figure 3.9a and 3.9b, respectively (Movies III and IV for details - Appendix). From the streamline length, it is clear that the protrusions deviate the flow more drastically than both the smoothed and perfectly smooth surfaces in either flow direction. The most evident distortion of flow is observed in the convoluted vorticities produced in the deep valleys of surface cavities, indicating that the tortuous drag near the surface of rough grains might facilitate the contact of colloids with the grains surface where attachment is likely to occur.

3.5. DISCUSSION

This study focuses on the effect of surface heterogeneity on fluid flow to provide an insight to the microfluidic dynamics that may be responsible for experimentally observed enhanced colloid retention on rough grain surfaces. Colloid retention has been previously ascribed to hydrodynamic driven processes, including: diffusion into regions of stagnant flow, straining in areas smaller than the colloid diameter, and trapping in vorticities [*Bradford et al.*, 2009; *Johnson et al.*, 2007a; *Zhang et al.*, 2010]. These retention sites are highly dependent on microfluidics which makes it evident that microfluidics plays a key role in colloid retention.

Stagnant flow regions have been experimentally and theoretically observed [*Gao et al.*, 2006; *Torkzaban et al.*, 2007] in which colloids are transferred from the mobile to the slow moving liquid phase of either dead end pores or near collector surfaces, where they can proceed to become attached if favorable conditions are met. The reduced hydrodynamic drag force in these regions may also provide optimum locations for the retention of colloids that are weakly associated with the surface by

the secondary energy minimum [*Bradford et al.*, 2007; *Bradford et al.*, 2006; *Torkzaban et al.*, 2007]. Set 1 simulations show that, in the case of a single grain, stagnant flow regions are always formed both in the front and rear of the grain (Figure 3.5). As illustrated in Figure 3.5b the presence of micron scale surface asperities (compared to perfectly smooth grains) generated additional stagnant flow regions in the pits of the grain surface. This can also be inferred from Figure 3.6 which illustrates the cumulative fractional areas having similar flow velocities in Figure 3.5. The relatively higher fraction of the areas having slower flow velocities in the simulation of naturally rough grain proves that the presence of surface asperities created more stagnant/low flow zones within the flow field which could result in retention of more colloids. Here it should be noted that Figures 3.5 only shows a 2-Dimensional cross sectional areas of the grains crossing the geometries from the middle points of the coordinate systems to present a clear illustration. If whole 3-Dimensional geometry is considered (data not shown), the effect of surface asperities is more substantial on the formation of stagnant/low flow regions. Such hydrodynamic regions could justify the experimental observations of increased colloid retention with grain surface properties reported by *Gao et al.* [2006], *Torkzaban et al.* [2007], and *Morales et al.* [2009].

It is inferred from the comparison of Figures 3.9 and 3.10 that vorticities formed near the surface of imperfect grains could significantly enhance colloid retention. The size and distribution of such vorticities along the imperfect grain is highly dependent on asperity size (i.e., width of cavity and peak-to-valley distance), uniformity of asperities, and the direction of the flow.

Colloids could become trapped on the grain surface, as suspended colloids swerve into surface cavities (i.e., strained in topographic valleys) by diverted streamlines [*Tong et*

al., 2008] (Supplementary Movie V in Appendix) as is evident in the streamlines of rough surfaces depicted in Figures 3.9 and 3.10. The hydrodynamic simulations indicate that this type of retention resembles the "wedging" or "straining" previously reported to occur at grain-to-grain contacts [*Bradford et al.*, 2009; *Tong et al.*, 2008; *Torkzaban et al.*, 2008], with the straining sites located on the surface of rough grains. In summary, flow hydrodynamics (as influenced by the micron-scale surface roughness) may account for the discrepancy between retention predictions from existing theories (e.g. CFT and DLVO) and experimental observations on non-ideal collectors. Near grain surface hydrodynamics of non-perfectly smooth collectors indicate that streamline deviations create stagnant flow regions and vorticities that that could loosely immobilize colloids, as well as drag particles close enough to the surface of the grain where under favorable conditions colloids can become permanently retained. It is likely that multiple scales of roughness operate in concert to facilitate colloid retention, as micron-scale asperities could help colloids become retained by influencing the near grain surface hydrodynamics (as presented in this study), while nano-scale roughnesses influence DLVO energy levels by allowing particle protrusions to extend beyond the electric double layer [*Hoek and Agarwal*, 2006; *Hoek et al.*, 2003; *Suresh and Walz*, 1996]. As such, the connection between near grain–surface hydrodynamics and colloid retention requires further work.

3.6. CONCLUSIONS

Computational simulations were done to assess the effect of surface asperities on hydrodynamics that could affect colloid transport behavior at the micron-scale. The simulations were divided into two sets to understand how micron-scale surface asperities may affect microhydrodynamics at pore scale (Set 1) and at surface scale (Set 2). It was found that surface asperities had profound effect on

microhydrodynamics that could lead the discrepancies between theoretical calculations and experimental findings in colloid transport studies. Specific findings are listed below.

- At the collector scale, micron-sized surface asperities lead to the formation of vorticities and enhanced stagnant/low flow spots around the near sand grain region.
- At the surface scale, it was observed that flow vorticities could also be formed among the asperities, where colloids could easily get trapped on the surface of a rough sand grain.
- The formation of vorticities was dependent on the direction of fluid flow.

It is believed that this information will help clarify the potential effect of micron-sized surface roughness on colloid behavior under favorable saturated conditions in porous media.

REFERENCES

Abuzeid, S., A. A. Busnaina, and G. Ahmadi (1991), Wall deposition of aerosol particles in a turbulent channel flow, *J. Aerosol Sci*, *22*(1), 43-62, doi: 10.1016/0021-8502(91)90092-v.

Adamczyk, Z., M. Adamczyk, and T. G. M. Van de Ven (1983), Resistance Coefficient of a Solid Sphere Approaching Plane and Curved Boundaries, *J. Colloid Interface Sci.*, *96*(1), 204-213.

Alshibli, K. A., and M. I. Alsaleh (2004), Characterizing surface roughness and shape of sands using digital microscopy, J Comput Civil Eng, 18(1), 36-45, doi: 10.1061/(Asce)0887-3801(2004)18:1(36).

Bradford, S. A., and S. Torkzaban (2008), Colloid transport and retention in unsaturated porous media: A review of interface-, collector-, and pore-scale processes and models, *Vadose Zone J.*, *7*(2), 667-681, doi: 10.2136/Vzj2007.0092.

Bradford, S. A., S. Torkzaban, and S. L. Walker (2007), Coupling of physical and chemical mechanisms of colloid straining in saturated porous media, *Water Res.*, *41*(13), 3012-3024, doi: 10.1016/j.watres.2007.03.030.

Bradford, S. A., J. Simunek, M. Bettahar, M. T. van Genuchten, and S. R. Yates (2006), Significance of straining in colloid deposition: Evidence and implications, *Water Resour. Res.*, *42*(12), W12S15, doi: 10.1029/2005wr004791.

Bradford, S. A., S. Torkzaban, F. Leij, J. Simunek, and M. T. van Genuchten (2009), Modeling the coupled effects of pore space geometry and velocity on colloid transport and retention, *Water Resour. Res.*, *45*, W02414, doi: 10.1029/2008wr007096.

Cakmak, M. E., B. Gao, J. L. Nieber, and T. S. Steenhuis (2008), Pore Scale Simulation of Colloid Deposition, in *Recent Advances in Modelling and Simulation*, edited by G. Petrone and G. Cammarata, p. 688, I-Tech Education and Publishing, Vienna.

Crist, J. T., Y. Zevi, J. F. McCarthy, J. A. Throop, and T. S. Steenhuis (2005), Transport and retention mechanisms of colloids in partially saturated porous media, *Vadose Zone J.*, *4*(1), 184-195.

Crist, J. T., J. F. McCarthy, Y. Zevi, P. Baveye, J. A. Throop, and T. S. Steenhuis

(2004), Pore-scale visualization of colloid transport and retention in partly saturated porous media, *Vadose Zone J.*, *3*(2), 444-450.
Cushing, R. S., and D. F. Lawler (1998), Depth filtration: Fundamental investigation through three dimensional trajectory analysis, *Environ. Sci. Technol.*, *32*(23), 3793-3801.
Elimelech, M., and C. R. Omelia (1990), Kinetics of Deposition of Colloidal Particles in Porous-Media, *Environ. Sci. Technol.*, *24*(10), 1528-1536.
Elimelech, M., J. Gregory, X. Jia, and R. A. Williams (1995), *Particle Deposition and Aggregation Measurement, Modelling and Simulation*, Butterworth-Heinemann, Oxford.
Fan, F.-G., and G. Ahmadi (1995), A sublayer model for wall deposition of ellipsoidal particles in turbulent streams, *J. Aerosol Sci*, *26*(5), 813-840, doi: 10.1016/0021-8502(95)00021-4.
Gao, B., J. E. Saiers, and J. Ryan (2006), Pore-scale mechanisms of colloid deposition and mobilization during steady and transient flow through unsaturated granular media, *Water Resour. Res.*, *42*(1), W01410, doi: 10.1029/2005wr004233.
Gao, B., T. S. Steenhuis, Y. Zevi, V. L. Morales, J. L. Nieber, B. K. Richards, J. F. McCarthy, and J. Y. Parlange (2008), Capillary retention of colloids in unsaturated porous media, *Water Resour. Res.*, *44*(4), W04504, doi: 10.1029/2006wr005332.
Grass, A. J., R. J. Stuart, and M. Mansour-Tehrani (1991), Vortical Structures and Coherent Motion in Turbulent Flow over Smooth and Rough Boundaries, *Philosophical Transactions of the Royal Society of London. Series A: Physical and Engineering Sciences*, *336*(1640), 35-65, doi: 10.1098/rsta.1991.0065.
Hahn, M. W., and C. R. O'Melia (2004), Deposition and reentrainment of Brownian particles in porous media under unfavorable chemical conditions: Some concepts and applications, *Environ. Sci. Technol.*, *38*(1), 210-220, doi: Doi 10.1021/Es030416n.
Hoek, E. M. V., and G. K. Agarwal (2006), Extended DLVO interactions between spherical particles and rough surfaces, *J. Colloid Interface Sci.*, *298*(1), 50-58, doi: 10.1016/j.jcis.2005.12.031.
Hoek, E. M. V., S. Bhattacharjee, and M. Elimelech (2003), Effect of membrane

surface roughness on colloid-membrane DLVO interactions, *Langmuir*, *19*(11), 4836-4847, doi: 10.1021/La027083c.

Johnson, W. P., M. Tong, and X. Li (2007a), On colloid retention in saturated porous media in the presence of energy barriers: The failure of alpha, and opportunities to predict eta, *Water Resour. Res.*, *43*(12), W12s13, doi: 10.1029/2006wr005770.

Johnson, W. P., X. Q. Li, and G. Yal (2007b), Colloid retention in porous media: Mechanistic confirmation of wedging and retention in zones of flow stagnation, *Environ. Sci. Technol.*, *41*(4), 1279-1287, doi: 10.1021/Es061301x.

Kemps, J. A. L., and S. Bhattacharjee (2009), Particle Tracking Model for Colloid Transport near Planar Surfaces Covered with Spherical Asperities, *Langmuir*, *25*(12), 6887-6897, doi: 10.1021/la9001835.

Li, A., and G. Ahmadi (1993), Deposition of aerosols on surfaces in a turbulent channel flow, *International Journal of Engineering Science*, *31*(3), 435-451, doi: 10.1016/0020-7225(93)90017-o.

Li, X., Z. Li, and D. Zhang (2010), Role of Low Flow and Backward Flow Zones on Colloid Transport in Pore Structures Derived from Real Porous Media, *Environ. Sci. Technol.*, *44*(13), 4936-4942, doi: 10.1021/es903647g.

Li, X. Q., C. L. Lin, J. D. Miller, and W. P. Johnson (2006), Role of grain-to-grain contacts on profiles of retained colloids in porous media in the presence of an energy barrier to deposition, *Environ. Sci. Technol.*, *40*(12), 3769-3774, doi: 10.1021/Es052501w.

Ma, H. L., J. Pedel, P. Fife, and W. P. Johnson (2009), Hemispheres-in-Cell Geometry to Predict Colloid Deposition in Porous Media, *Environ. Sci. Technol.*, *43*(22), 8573-8579, doi: 10.1021/Es901242b.

McBride, M. B. (1997), A critique of diffuse double layer models applied to colloid and surface chemistry, *Clays Clay Miner.*, *45*(4), 598-608.

McCarthy, J. F., and L. D. McKay (2004), Colloid transport in the subsurface: Past, present, and future challenges, *Vadose Zone J.*, *3*(2), 326-337.

Morales, V. L., B. Gao, and T. S. Steenhuis (2009), Grain Surface-Roughness Effects on Colloidal Retention in the Vadose Zone, *Vadose Zone J.*, *8*(1), 11-20, doi:

10.2136/Vzj2007.0171.
Morrison, J. F., C. S. Subramanian, and P. Bradshaw (1992), Bursts and the law of the wall in turbulent boundary layers, *J. Fluid Mech.*, *241*(-1), 75-108, doi: 10.1017/S0022112092001952.
Ounis, H., G. Ahmadi, and J. B. McLaughlin (1991), Dispersion and deposition of Brownian particles from point sources in a simulated turbulent channel flow, *J. Colloid Interface Sci.*, *147*(1), 233-250, doi: 10.1016/0021-9797(91)90151-w.
Rajagopalan, R., and C. Tien (1976), Trajectory Analysis of Deep-Bed Filtration with Sphere-in-Cell Porous-Media Model, *AlChE J.*, *22*(3), 523-533.
Ryan, J. N., and M. Elimelech (1996), Colloid mobilization and transport in groundwater, *Colloids Surf., A*, *107*, 1-56.
Saiers, J. E., and J. N. Ryan (2005), Colloid deposition on non-ideal porous media: The influences of collector shape and roughness on the single-collector efficiency, *Geophys. Res. Lett.*, *32*(21), L21406, doi: 10.1029/2005gl024343.
Shellenberger, K., and B. E. Logan (2002), Effect of molecular scale roughness of glass beads on colloidal and bacterial deposition, *Environ. Sci. Technol.*, *36*(2), 184-189, doi: 10.1021/Es015515k.
Shi, X.-Y., H. Gao, V. I. Lazouskaya, Q. Kang, Y. Jin, and L.-P. Wang (2010), Viscous flow and colloid transport near air-water interface in a microchannel, *Comput Math Appl*, *59*(7), 2290-2304, doi: 10.1016/j.camwa.2009.08.059.
Suresh, L., and J. Y. Walz (1996), Effect of surface roughness on the interaction energy between a colloidal sphere and a flat plate, *J. Colloid Interface Sci.*, *183*(1), 199-213.
Tien, C., and B. V. Ramarao (2007), *Granular Filtration of Aerosols and Hydrosols*, 2nd ed., Butterworth-Heinemann, Great Britain.
Tobiason, J. E. (1989), Chemical Effects on the Deposition of Non-Brownian Particles, *Colloids Surf.*, *39*(1-3), 53-77.
Tong, M. P., H. L. Ma, and W. P. Johnson (2008), Funneling of flow into grain-to-grain contacts drives colloid-colloid aggregation in the presence of an energy barrier, *Environ. Sci. Technol.*, *42*(8), 2826-2832, doi: 10.1021/Es071888v.

Torkzaban, S., S. A. Bradford, and S. L. Walker (2007), Resolving the coupled effects of hydrodynamics and DLVO forces on colloid attachment in porous media, *Langmuir*, *23*(19), 9652-9660, doi: 10.1021/1a700995e.

Torkzaban, S., S. S. Tazehkand, S. L. Walker, and S. A. Bradford (2008), Transport and fate of bacteria in porous media: Coupled effects of chemical conditions and pore space geometry, *Water Resour. Res.*, *44*(4), W04403, doi: 10.1029/2007wr006541.

Tosun, I. (2002), *Modeling in transport phenomena a conceptual approach*, 1st ed., Elsevier, Amsterdam.

Tufenkji, N., and M. Elimelech (2004), Correlation equation for predicting single-collector efficiency in physicochemical filtration in saturated porous media, *Environ. Sci. Technol.*, *38*(2), 529-536, doi: Doi 10.1021/Es034049r.

Wan, J. M., and J. L. Wilson (1994), Visualization of the Role of the Gas-Water Interface on the Fate and Transport of Colloids in Porous-Media, *Water Resour. Res.*, *30*(1), 11-23.

Wan, J. M., and T. K. Tokunaga (1997), Film straining of colloids in unsaturated porous media: Conceptual model and experimental testing, *Environ. Sci. Technol.*, *31*(8), 2413-2420.

Yao, K. M., M. M. Habibian, and C. R. Omelia (1971), Water and Waste Water Filtration - Concepts and Applications, *Environ. Sci. Technol.*, *5*(11), 1105-1112.

Zevi, Y., A. Dathe, J. F. Mccarthy, B. K. Richards, and T. S. Steenhuis (2005), Distribution of colloid particles onto interfaces in partially saturated sand, *Environ. Sci. Technol.*, *39*(18), 7055-7064, doi: 10.1021/Es048595b.

Zhang, W., V. n. L. Morales, M. E. Cakmak, A. E. Salvucci, L. D. Geohring, A. G. Hay, J.-Y. Parlange, and T. S. Steenhuis (2010), Colloid Transport and Retention in Unsaturated Porous Media: Effect of Colloid Input Concentration, *Environ. Sci. Technol.*, *44*(13), 4965-4972, doi: 10.1021/es100272f.

CHAPTER 4
SIMULATION OF DYNAMIC CONTACT ANGLES IN PORES: HOFFMAN (1975) REVISITED

4.1. ABSTRACT

The dynamic behavior of the contact angles at the wetting front in soils is one of the outstanding issues is that is not fully resolved. Since Richards' equation assumes that the contact angle is time invariant, gaining this knowledge is important. To obtain a better understanding how contact angles vary, we simulated the upward movement of a liquid in a capillary pore by solving the incompressible Navier-Stokes equation with finite element method. Initial contact angles of 40 and 90 degrees were simulated. Pressure gradients of 5 to 3000 Pa were imposed resulting in velocities of the wetting front ranging from 6.80×10^{-4} to 6.82×10^{-3} m/s. Simulated contact angles were compared to *Hoffman* [1975] experimental results done in a horizontal column and our experiments. For increasing pore velocities for the same liquid, contact angle remained equal to the initially imposed contact angles for small velocities and then increased with increasing pore velocities for the same liquid as *Hoffman* [1975] observed. Deviations from the Hoffman results occurred for cases when gravity or inertial forces could not be neglected. This occurred at low and very high velocities of the liquid.

4.2. INTRODUCTION

Elucidating factors (e.g., hydraulic conductivity, infiltration rate) and forces (e.g., capillary, viscous, and gravitational forces) affecting the dynamics and stability of wetting front is of interest for many processes including prediction of enhanced oil recovery from oil reservoirs and infiltration of water into porous media as column flow. Literature finding show that under variable gravity when during drainage the

gravitational forces dominate capillary forces a stable displacement was observed, whereas when capillary forces gradually become dominant instability increasingly occurred. [*DiCarlo et al.*, 2000; *Hillel*, 1987; *Or*, 2008; *Or et al.* 2009; *de Rooij*, 2000; *Kordel et al.*, 2008]. Wetting front instability has been related to dynamically varying liquid-air contact angles [*Blake*, 2006; *Degennes*, 1985; *Raats*, 1973]. *DiCarlo* [2010] and *Hendrickx* et al [1996] observed that decreasing fluxes resulted in less fingering.

The interaction of fluid flow velocity (and more precisely the contact line between the two liquids) and contact angle in a small capillary tube has been examined by *Dussan* [1979] and *Degennes* [1985]. Unlike the general soil physics theory, the contact angle varied greatly as a function of contact line velocity and surface tension [*Degennes*, 1985; *Dussan*, 1979]. Especially the effect of contact line velocity on contact angle deviation from the static contact angle was well presented by *Hoffman* [1975]. In his experimental study, the dynamic contact angle was measured for five different fluids in a horizontal channel (without gravitational force) were examined by dimensionless numbers, namely Capillary (*Ca*) (the ratio of viscous to capillary forces) and Weber (*We*) (the ratio of inertial to capillary forces) numbers. The effect of inertial forces was intentionally kept negligible ($5.4\times10^{-11} \leq We \leq 1\times10^{-5}$) to only account for the influence of capillary and viscous forces ($4\times10^{-5} \leq Ca \leq 36$). The deviation of the dynamic contact angle from the static contact angle was correlated to the capillary number along with a shift factor when the interfacial (capillary) and viscous forces were controlling the system. In addition, the data indicating the dependence of dynamic contact angle on contact line velocity over the complete range of contact angles ($0^{o} \leq \theta_a \leq 180\ ^{o}$).

To elucidate the effect of both the contact line velocity and the relative importance of capillary, gravitational, viscous forces on wetting front several studies were carried out subsequently to Hoffman's pioneering work. *Or* [2008] concluded that when the Bond Number was larger than the Capillary Number stable flow occurs and Richards' equation can be used. In the remaining cases unstable flow may occur. In a follow up study on the effect of Bond and Capillary Numbers on fluid stability by *Lunati and Or* [2009], gravitational movement of a fluid slug in a capillary tube was simulated by numerically solving the Navier-Stokes equation using the volume of fluid method (VOF). With VOF method the mass of the fluid is conserved but not very well the meniscus shape, whereas the level set method (used in this study) is preferred for simulating the interface shape and contact angle [*Olsson and Kreiss*, 2005]. *Chebbi* [2003] solved the Stokes equations without gravitational force for contact angles close to the static angle (in a range of 4 to 40 degrees). In another numerical simulation study in a horizontal cylindrical tube by *dos Santos et al.* [2005], using the Lattice-Boltzmann method dynamic contact angle increased with increasing velocity.

In 2006 Blake noted that substantial contributions had been made to the knowledge of dynamic wetting, practical and reliable numerical simulations was lacking. Only recently both sufficient computational power and reliable numerical methods have been become available for simulating the shape of contact line and contact angle in pores. . Therefore in this study we use the latest software by COMSOL that is optimized for calculations to study the dependence of dynamic contact angle on contact line velocity in a vertical capillary tube with gravity opposite the flow direction. The numerical solution is compared with the experimental results of *Hoffman* [1975].

4.3. MATERIAL AND METHODS

The dependence of dynamic contact angle on contact line velocity was assessed both numerically and experimentally.

Numerical simulations: The change in dynamic contact angle by changing contact line velocity was assessed by simulating upward advancing of a dense liquid into air in a capillary tube with a diameter of 0.15 mm under the opposite influence of the gravitational force in axis-symmetrical plane. Simulations were done by numerically solving the incompressible Navier-Stokes and level set equations with COMSOL Multiphysics, a simulation program based on finite element method. In addition, the dynamics of glycerin-air contact line in a capillary channel was visualized to also experimentally validate the simulated results.

In the simulations the physical properties of the liquid was chosen to be that of G.E. Silicone Fluid SF-96, which was one of the liquids used by *Hoffman* [1975]. It has a density of 960 kg/m^3 and a viscosity of 0.958 Pa·s. The surface tension between air and the liquid is 2.13×10^{-2} N/m. The geometry used in the simulations was consisted of two parts, i.e., the capillary channel and the base (Figure 4.1). This configuration was chosen because it was optimized by COMSOL for these types of experiments. The flow velocity was changed by specifying varying pressures on the liquid at the inlet of the base. While the height of the channel was changed from 0.5 to 7.5 mm in order to reach steady state for each contact line velocity, the dimensions of the rectangular base were kept constant (0.15 mm × 0.30 mm). The mesh systems including the base for each channel length constructed of square elements with side size of 5×10^{-6} m. This meshing method resulted in 12,000 to 46,800 total mesh elements in the whole geometry depending on the length of the channel. A meshed

representation of the geometry with 12,000 square elements used in the simulations is illustrated in Figure 4.1a.

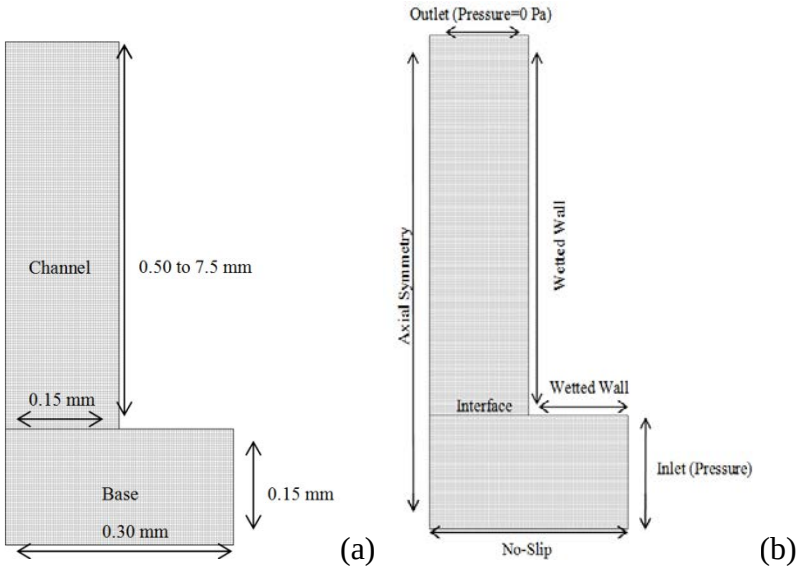

Figure 4.1. The representation of the geometry and boundary conditions

Dynamic contact line simulations were performed numerically based on finite element method using COMSOL Multiphysics® v3.5a (COMSOL, Inc., Burlington, MA, USA). COMSOL has two different methods to simulate flow of two immiscible liquids, i.e. level set and volume of fluid, the level set method was chosen because it is easier to track dynamic contact line and it gives more accurate results for contact angle, whereas volume of fluid method is better for conservation of mass to determine deformation of interfaces. The level set method used in this study incorporates the solution of the incompressible Navier-Stokes Equation (Equation 4.1 and 4.2) and a level set function (Equation 4.3) for each phase (i.e., gas and liquid) on the contact line:

$$\rho\left(\frac{\partial v}{\partial t}+v\cdot\nabla v\right)=-\nabla p+\mu\,\nabla^2 v+F \qquad (4.1)$$

$$\nabla \cdot v = 0 \tag{4.2}$$

$$\frac{\partial \phi}{\partial t} + v \cdot \nabla \phi = \gamma \nabla \cdot \left(\varepsilon \nabla \phi - \phi \left(1 - \phi \right) \frac{\nabla \phi}{|\nabla \phi|} \right) \tag{4.3}$$

where ρ is the density of the fluid (kg/m^3), v is the fluid velocity (m/s), t is the time (s), p is the pressure (Pa), μ is the dynamic viscosity of the fluid (Pa.s), F is gravitational force and $F=\rho g$), g is the gravitational acceleration (9.81 m^2/s), For numerical stability two parameters are used : ϕ is the level set function which takes values from 0 to 1 along the contact line according to the percentage of the dominant phase (i.e. water and air), γ is the interface thickness and ε is a reinitialization parameter. The parameter ε is usually taken as the half of the maximum element size and is equal to 5×10^{-6} meters in our simulations and γ is an approximate value of the maximum speed occurring in the flow was taken as 1×10^{-2} m/s in our simulations).

The boundary conditions for a cylindrical channel and the reservoir base are depicted in Figure 4.1b. The left side was specified as axial-symmetry boundary. The bottom of the base was a no-slip boundary with zero velocity at the wall surface. The right side of the channel and the upper right part of the base were specified as wetted wall boundary The wetted wall conditions in COMSOL is composed of an imaginary no slip boundary which is located one mesh element (5×10^{-6} m in our simulations) from the wall boundary. In addition the normal component of the velocity is zero and the tangential component of the total stress is zero.

Simulations were run for static contact angles of 40º and 90º. These contact angles were imposed at the imaginary boundary. For the simulations with the static angle of

40º pressures on the liquid at the base were 25, 300, 1000, and 1500 Pa and for the 90º the pressures imposed were 5, 25, 50, 100, 300, 1000, and 3000 Pa. To assure stable fluid potentials, the column height was increased from 0.5 mm to 7.5 mm for pressures imposed at the base greater than 300 Pa.

For presenting the results, the contact line was taken as interface boundary where normal component of the total stress is zero. Contact line velocities were determined by calculating the distance that the contact line moved for two subsequent times. Contact angle was calculated by taking arccosine of normal component of the interface. Each simulation took approximately 10-20 days depending on the length of the column and imposed pressure (i.e. contact line velocity).

Experimental observations: The contact angles were observed with the bright field microscope (BFM) (KH-7700 Hirox-USA, River Edge, NJ) in a capillary channel. The inner dimensions of rectangular capillary tube (Borosilicate, Friedrich & Dimmock, Inc., Millville, NJ) were 3 mm x 9 mm x 203 mm. The 20x objective lens was used, yielding the image resolution of 10.3 μm/pixel. The capillary tube was mounted at different inclination angles to alternate the liquid velocity (Figure 4.2). Glycerin with viscosity of 1.49 Pa·s and density of 1261 kg/m^3 at (20ºC) was used. Surface tension of glycerin/air interface was taken to be 6.4×10^{-2} N/m.

Glycerin was injected horizontally into the capillary tube. While horizontal, the ends are capped so glycerin does not move while being placed on the stand due to air entrapment. The microscope was tilted to offset the inclination of the capillary tube. The capillary tube was cleaned using high pressure distilled water, followed by a rinse using an 95% ethyl alcohol solution and a drying oven. The capillary tube was tilted at

different inclination angles to change the velocity of glycerin.

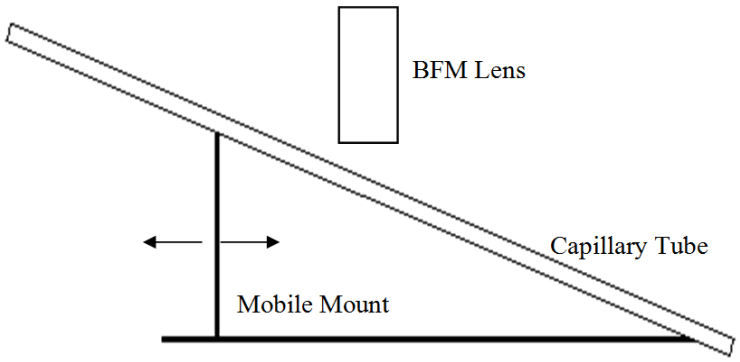

Figure 4.2. Depiction of the experimental setup used

To measure contact angles continuously taken digital images of dynamic meniscus were enlarged by using an image processing software, ImageJ. The edges of the contact line were digitally located, and then the contact angles were manually measured by marking the angle on a screen within the ImageJ program.

4.4. RESULTS

The imposed pressure at the base and the simulated velocity of the front and the dynamic contact angle at are summarized in Table 4.1. In the simulations and the data from the experiment, the dynamic contact angle remains close to the initial static contact angle for small velocities. Once the velocity become larger than around 1 mm/s, the dynamic contact angle increases with increasing velocities.

The shape of the contact line was measured after the contact line profile stabilized. It is of interest to see how the contact line changes as a function of time after the start of the simulation. As an example we use the simulation with a static contact angle of 40º with imposed pressure at the base of 300 Pa (Figure 4.3). At time t = 0 when the simulation starts the contact line is flat (not shown). At 0.01 sec the contact line is

convex because in the middle of the tube has the least resistance to flow and hence the convex shape of the contact line. Subsequently the contact angle decreases and after approximately 0.1 seconds, the contact line stabilizes. The rather fast changing contact line before it reaches the "stable" configuration is caused by the inertial forces in the liquid. Note that the contact angle (and velocity) for t=0.125 second is reported in table 4.1.

Table 4.1. The results showing variance of the dimensionless numbers with varying contact line velocities and initially imposed pressures.

θ_s	θ_a	v (m/s)	Ca ($\mu v/\sigma$)	We ($\rho v^2 a/\sigma$)	Fr (v^2/ga)	P (Pa)
40º	40	1.20E-05	5.40E-04	9.74E-10	9.79E-08	0
	59	1.25E-03	5.63E-02	5.31E-06	2.13E-03	25
	65	2.22E-03	1.00E-01	1.67E-05	6.71E-03	300
	136	6.32E-03	2.84E-01	1.35E-04	5.43E-02	1000
	158	6.82E-03	3.07E-01	1.57E-04	6.32E-02	1500
90º	90	1.68E-05	7.56E-04	9.54E-10	3.84E-07	5
	91	1.16E-04	5.22E-03	4.55E-08	1.83E-05	25
	93	1.62E-04	7.29E-03	8.87E-08	3.57E-05	50
	97	4.64E-04	2.09E-02	7.28E-07	2.93E-04	100
	127	1.58E-03	7.11E-02	8.44E-06	3.39E-03	300
	164	4.72E-03	2.12E-01	7.53E-05	3.03E-02	1000
	179	5.23E-03	2.35E-01	1.85E-04	1.86E-02	3000
Glycerin	89	4.36E-05	8.17E-04	5.61E-08	1.29E-07	N/A
	87	7.07E-04	1.33E-02	1.48E-05	3.39E-05	N/A
	100	9.37E-04	1.76E-02	2.60E-05	5.97E-05	N/A
	113	1.15E-03	2.16E-02	3.93E-05	9.04E-05	N/A

θ_s: Imposed static contact angle, θ_a: dynamic contact angle P: Imposed pressure on the liquid phase at the base

In order to compare our results with those in the literature, we employ the non-dimensional Capillary (*Ca*), Weber (*We*), Froude (*Fr*), and Bond (B*o*) numbers, which are defined as follows:

$$Ca = \frac{\mu v}{\sigma} \tag{4.4}$$

$$We = \frac{\rho v^2 a}{\sigma} \tag{4.5}$$

$$Fr = \frac{v^2}{g a} \tag{4.6}$$

$$Bo = \frac{\rho g a^2}{\sigma} \tag{4.7}$$

where μ is the viscosity, v is the velocity, σ is the surface tension (N/m), ρ is the density of the fluid (kg/m^3), a is the characteristic length (radius of the channel) (m).

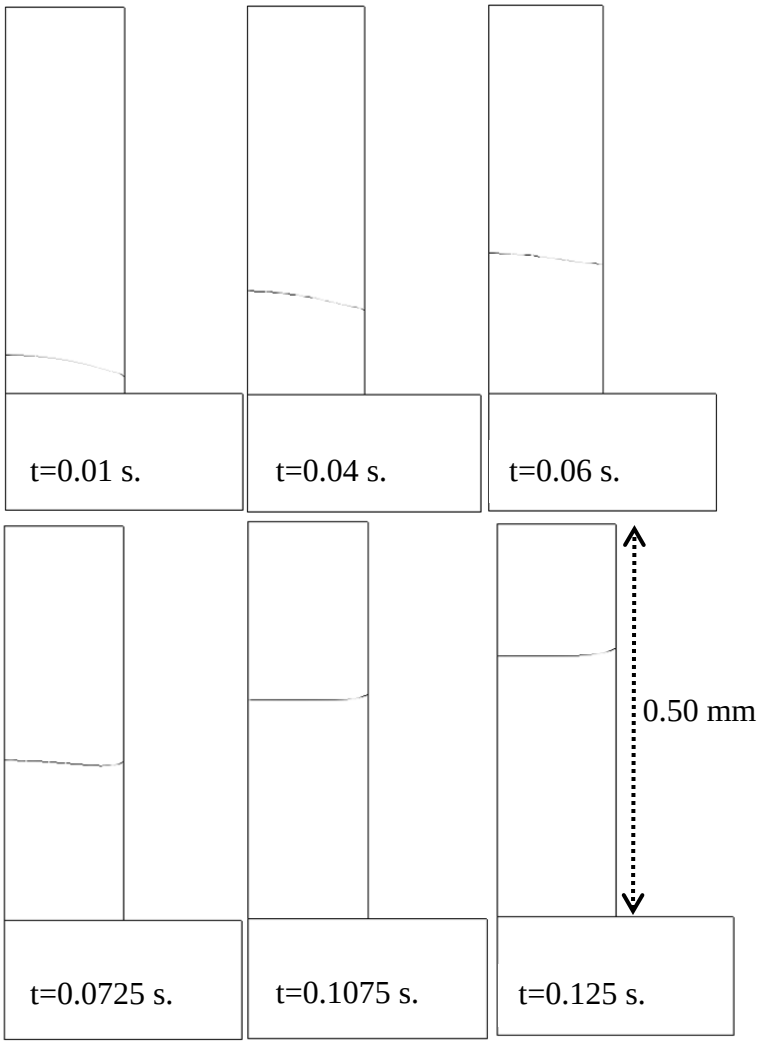

Figure 4.3. Contact line shape development for a static contact angle of 40º and imposed pressure of 300 Pa at the reservoir base.

The simulated and experimentally dynamic contact angles are shown in Figures 4.4 through 4.6 as a function of the Capillary (*Ca*), Weber (*We*), and Froude (*Fr*) respectively. In the same graphs, the dynamic contact angle data of *Hoffman* [1975] and *dos Santos et al.* [2005] are plotted. The Hoffman data used five different liquids and cover the whole range of 0º to 180º while *dos Santos et al.* [2005] data were obtained by simulation using the Lattice-Boltzmann technique. The range of the *dos Santos et al.* [2005] dynamic contact angles was from 11º to 40º

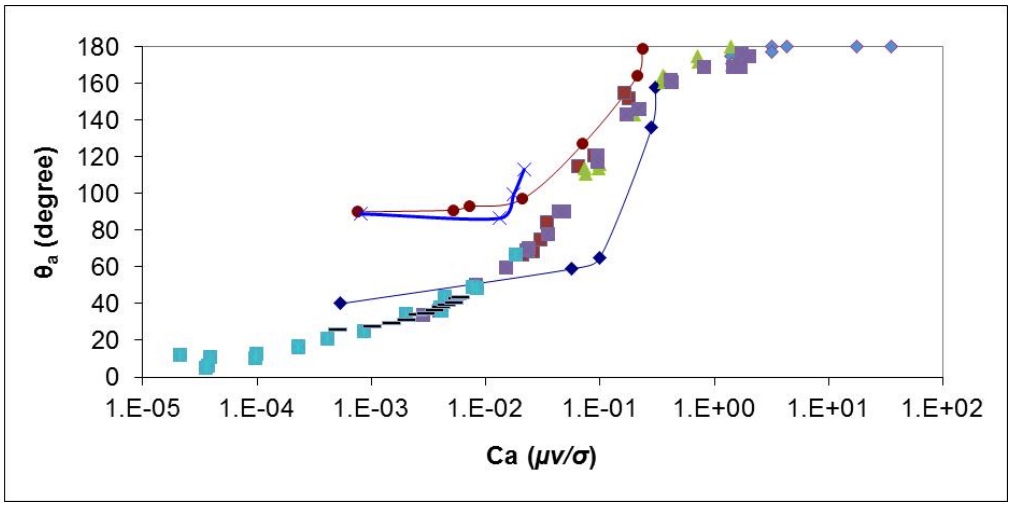

Figure 4.4. The change in dynamic contact angle (θ_a) against Capillary number (Ca) Initially imposed contact angles (♦) 40º, (●) 90º, and (×) experiment with glycerin. The S shaped curve is Hoffman's results obtained using five different fluids: (■) G.E. Silicone Fluid SF-96, (■) Brookfield Std. Viscosity Fluid, (♦) Dow Corning 200, (▲) Ashland Chem. Admex 760, (■) Santicizer 405. And (—) the results of *dos Santos et al.*[2005].

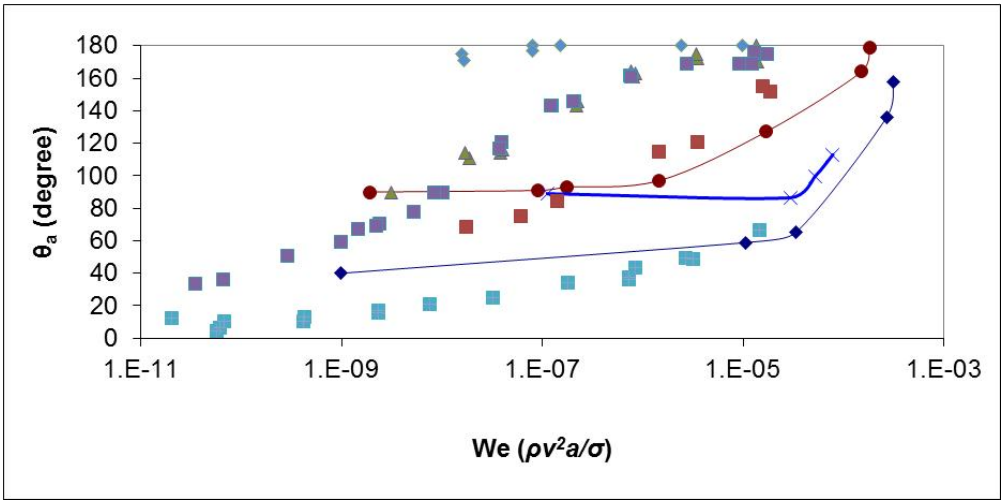

Figure 4.5. Illustration of the relation between dynamic contact angle (θ_a) and Weber (We) number. Initially imposed contact angles (♦) 40º, (●) 90º, and (×) experiment with glycerin. Hoffman's results obtained using five different fluids: (■) G.E. Silicone Fluid SF-96, (■) Brookfield Std. Viscosity Fluid, (♦) Dow Corning 200, (▲) Ashland Chem. Admex 760, (■) Santicizer 405

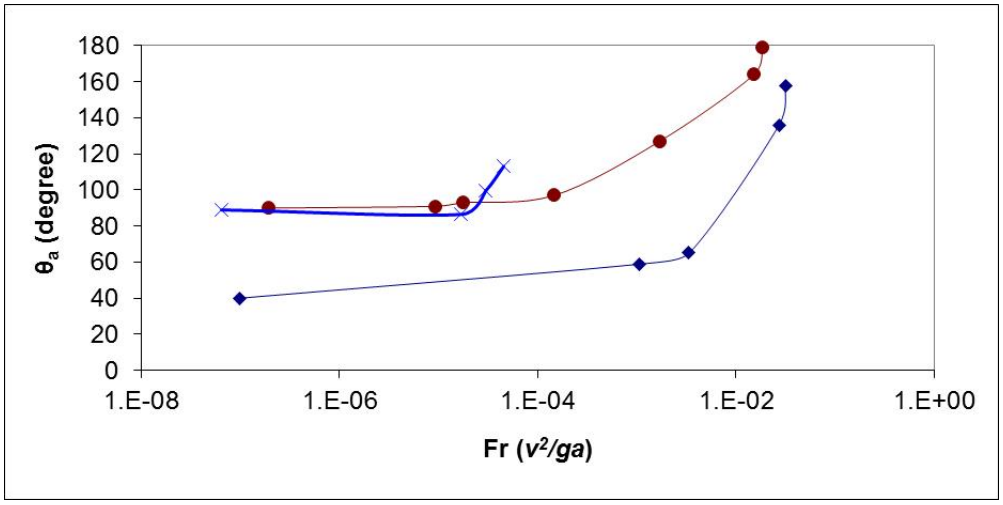

Figure 4.6. The connection between dynamic contact angle (θ_a) and Froude (Fr) number. Initially imposed contact angles (♦) 40º, (●) 90º, and (×) experiment with glycerin. Hoffman's results obtained using five different fluids: (■) G.E. Silicone Fluid SF-96, (■) Brookfield Std. Viscosity Fluid, (♦) Dow Corning 200, (▲) Ashland Chem. Admex 760, (■) Santicizer 405

In Figure 4.4 where the dynamic contact angles are plotted as a function of the capillary number, the simulated dynamic contact angles are constant and approximately equal to the static contact angle for small capillary numbers. When the coordinates for the capillary number and dynamic contact angle are similar to that for the Hoffman data in Figure 4.4 the contact angle increases with increasing capillary number. This is true for both the static contact angles of 40º and 90º and for the experimentally observed data with glycerin although the starting points vary slightly. Once increasing, the simulated data approach the Hoffman curve. The exceptions are the date point near the 180º line where the simulated data intersect the line at a 90º angle while the Hoffman data approach the 180º line asymptotically.

When the contact angles are plotted as a function of the Weber number in Figure 4.5, the experimental data of Hofmann for the different fluids are, as expected, not continuous. Hoffman neglected the inertia effect and used therefore only the points with Weber numbers less than 10^{-5} (Figure 4.5). The Weber numbers for the simulated data for pressures of 1000 Pa or more are in the order of 10^{-4} (table 4.1). Inertial effects cannot be neglected for these points as we will see later.

The viscosity and surface tension of the liquids used in the simulation were similar to Silicone (closed squares, Figure 4.5) but with a larger static contact angle in the simulations. When the dynamic contact angle of Silicone became equal to the 40º static contact angle of the simulated silicone liquid, the curves coincides. Figure 4.5 indicates that for greater velocities the simulated curve is a continuation of the Hoffman's Silicone curve.

In Figure 4.6, the simulated dynamic contact angles are plotted as a function of the Froude number. Since Hoffman did his experiment in horizontal columns, the Froude number was undefined. For the glycerin experiment the chamber was inclined at various rates and therefore the Froude numbers are difficult to determine. The main point of this graph is too show that at high velocities the Froude number increases and the gravity term becomes less important

The Bond number was 33.1 in the computer simulation contact angles and 290 for our glycerin experiment. The Bond numbers for the Hoffman liquids were 438.5, 431.7, 214.6, 525.1, 249.7 for G.E. Silicone Fluid SF-96, Brookfield Std. Viscosity Fluid, Dow Corning 200, Ashland Chem. Admex 760, and Santicizer 405, respectively.

4.5. DISCUSSION

Our simulated and experimental data follow partly of the Hoffman curve when plotted as a function of the Capillary number (Figure 4.4). However at both ends our results deviate from the *Hoffman* [1975] and *dos Santos* [2005]. The reasons are given below.

Hoffman did his experiment in a horizontal column avoiding gravity effect (i.e., Froude number is undefined). In addition, only the experimental data of the five liquids were used for which the Weber number was small. This means that Hoffman avoided the inertial effects as well. In our experiments the column was vertical or tilted and thus gravity played a role. In addition the Weber number was too high for pressures impose at the base of 1000 Pa or greater (Figure 4.5, Table 4.1).

The importance of the gravity effects on the contact angle dynamics can best be understood from the example that when the contact angle is static (i.e., the velocity of the liquid is zero) the capillary forces are balanced by the gravity forces. For both the glycerin and the simulated data (90º static contact angle) the dynamic contact angle is equal to the static contact angle for Froude number less than approximately 10^{-5} (Figure 4.6). Hence gravity dominates. The simulated data with the 40º are too coarse in this region to be conclusive. As we can see from Figure 4.4 and table 4.1 it is the points with small Froude numbers that deviate from the Hoffman curve. In other words, the Froude number need to be in excess 10^{-5} for the contact angle to follow the Hoffman curve.

Inertial effect on the dynamic contact becomes significant for large Weber numbers. Table 4.1 shows that Weber Numbers are in the order of 10^{-4} for the simulation with pressure 1000 Pa or larger at the reservoir base. The contact angles for these large Weber numbers are greater than 136º and pore water velocities are in the order of 5mm/sec (Table 4.1).

It is interesting to note that the Capillary number is much greater than the Bowen number, indicates that the contact line behavior was stable [*Or*, 2008; *Lunati and Or*, 2009]. More importantly our results confirm Hoffman's finding that the dynamic contact angle in pores is related to the Capillary number when the Froude number are large (in excess of 10^{-5}) and the Weber number is small (less than 10^{-5}).

Finally, it is important to relate back these results in this paper to real porous media and the applicability of Richards' equation at the wetting front. The velocities in the experiments discussed above are out of the range of spatial averaged velocities that

can be found realistically in soils. However, when we realize that at the wetting front in a dry soils, the average velocity is meaningless because water is released from each pore subsequently and not at the same time, the capillary numbers at the wetting front can be in the range of Hoffman. Thus, contact angles will not remain static when pores empty one at the time. In this case Richards' equation is not valid at the front. Thus ironically whether Richards equation applies at the wetting front or not depends on how many pores release water simultaneously at the front which is in accordance with the findings of DiCarlo (2010) that pressure overshoots occur in dry soils but not in wet soils.

REFERENCES

Blake, T. D. (2006), The physics of moving wetting lines, *J. Colloid Interface Sci.*, *299*(1), 1-13, doi: 10.1016/j.jcis.2006.03.051.

Chebbi, R. (2003), Deformation of advancing gas-liquid interfaces in capillary tubes, *J. Colloid Interface Sci.*, *265*(1), 166-173, doi: Doi 10.1016/S0021-9797(03)00415-6.

de Rooij, G. H. (2000), Modeling fingered flow of water in soils owing to wetting front instability: a review, *J Hydrol*, *231*, 277-294.

Degennes, P. G. (1985), Wetting: statics and dynamics, *Reviews of Modern Physics*, *57*(3), 827-863.

DiCarlo, D. A. (2010), Can Continuum Extensions to Multiphase Flow Models Describe Preferential Flow?, *Vadose Zone J.*, 9(2), 268-277, doi: 10.2136/Vzj2009.0099.

DiCarlo, D. A., A. Sahni, and M. J. Blunt (2000), Three-phase relative permeability of water-wet, oil-wet, and mixed-wet sandpacks, *Spe J*, *5*(1), 82-91.

dos Santos, L. O. E., F. G. Wolf, and P. C. Philippi (2005), Dynamics of interface displacement in capillary flow, *Journal of Statistical Physics*, *121*(1-2), 197-207, doi: 10.1007/s10955-005-7001-6.

Dussan, E. B. (1979), Spreading of liquids on solid-surfaces: static and dynamic contact lines, *Annual Review of Fluid Mechanics*, *11*, 371-400.

Hendrickx, J. M. H., and T. M. Yao (1996), Prediction of wetting front stability in dry field soils using soil and precipitation data, *Geoderma*, *70*(2-4), 265-280.

Hillel, D. (1987), Unstable flow in layered soils: a review, *Hydrol Process*, *1*(2), 143-147.

Hoffman, R. L. (1975), A study of advancing interface .1. Interface shape in liquid-gas systems, *J. Colloid Interface Sci.*, *50*(2), 228-241.

Kordel, W., H. Egli, and M. Klein (2008), Transport of pesticides via macropores (IUPAC technical report), *Pure Appl. Chem.*, *80*(1), 105-160, doi: 10.1351/pac200880010105.

Lunati, I., and D. Or (2009), Gravity-driven slug motion in capillary tubes, *Phys Fluids*, *21*(5), Artn 052003, doi: 10.1063/1.3125262.

Olsson, E., and G. Kreiss (2005), A conservative level set method for two phase flow, *Journal of Computational Physics, 210*(1), 225-246, doi: 10.1016/j.jcp.2005.04.007.
Or, D. (2008), Scaling of capillary, gravity and viscous forces affecting flow morphology in unsaturated porous media, *Adv Water Resour, 31*(9), 1129-1136.
Or, D., M. Tuller, and S. B. Jones (2009), Liquid Behavior in Partially Saturated Porous Media under Variable Gravity, *Soil Sci. Soc. Am. J., 73*(2), 341-350, doi: 10.2136/sssaj2008.0046.
Raats, P. A. C. (1973), Unstable wetting fronts in uniform and nonuniform soils, *Soil Sci Soc Am J, 37*(5), 681-685.

CHAPTER 5
CLOSING REMARKS AND FUTURE DIRECTIONS

5.1. CLOSING REMARKS

In this dissertation we aimed to elucidate the possible effects of hydrodynamics on transport in porous media. The second chapter helped us validate COMSOL's results against previous studies and test COMSOL's abilities. Although it was very easy to build and to mesh complex geometries with COMSOL, its need for high computational resources was our main limitation. While working on the second chapter the computer used in our simulations had 4 GB of memory and a Dual Core Processor. We both used Linux (Fedora 8 - 64 Bit) and Windows XP (64 Bit) operating systems. For mathematical calculations Linux had the advantage over XP, but for visualizations XP had the advantage. So we decided to use a dual booting the computer.

In the research process of the third chapter we upgraded the computer to 8 GB of memory which helped reduce computing time. The most important limitation encountered in the study was the meshing of 3-Dimensional (3-D) irregular volumes. This problem was overcome by many trials and errors in building the 3-D geometries. Although there had been many studies on the effect of surface roughness on hydrodynamics, none had explicitly shown the hydrodynamic pathways that could help explain colloid retention over rough surfaces.

The computational time was dramatically reduced by upgrading the computer to have 16 GB of memory and a Quad Core processor. Here it should be noted that we could

not use COMSOL on High Performance Computers (HPCs) because these HPCs did not allow real time monitoring of the computing and meshing processes and the huge file sizes changing from 5 MB to 15 GB were not suitable for data transferring from these remote systems.

The latest upgrade of the computer and using Windows 7 Pro (64 Bit) enabled us to fine-tune the simulations involved in third chapter and to go on to our last study on the simulation of dynamic contact angle. In the last chapter we simulated the dependence of dynamic contact angle on contact line velocity with a gravity effect that was not considered in previous studies. Our simulations were consistent with previous studies.

5.2. FUTURE DIRECTIONS

In the second chapter we would like to assess not only the classical colloid filtration theory but also the other models describing colloid retention in porous media. Because of the time limitation we were not able to do that. However, we will revisit the existing models such as Happel, Kuwabara, and Brinkman's models to see the possible differences between an axisymetrical and a real 3-D geometry.

We could not add the colloidal particles in the simulation of third chapter because of COMSOL's particle tracing module with which DLVO and hydrodynamic retardation forces cannot be considered due to lack of proper variable for approaching angle and distance for each colloidal particle. Nonetheless we are planning to use programming codes for particle tracing and we do not have to worry about flow field because the flow filed produced by COMSOL can be used.

In the fourth chapter only one liquid with two different initial contact angles could be

simulated because of time limitation. To obtain better insight into the behavior of dynamic contact angle we are planning to do simulations with different liquid properties and initial contact angles. We also plan to relate our findings with that of DiCarlo's experimental observation [*DiCarlo*, 2010] for unstable finger formation with a range of imposed fluxes.

REFERENCES

DiCarlo, D. A. (2010), Can Continuum Extensions to Multiphase Flow Models Describe Preferential Flow?, Vadose Zone J., 9(2), 268-277, doi: 10.2136/Vzj2009.0099.

APPENDIX

A1. GRAIN SURFACES

Images of the surface topography of randomly-selected smoothed (by lapidary tumbling) and naturally rough sand grains (0.6 mm mean diameter) from Morales et al. [2009] were used to digitally create realistic grain surface properties for the simulations. Close-up surface topography images of sand grain surfaces in Figures 3.1 and 3.2 (smoothed and naturally rough sand surfaces, respectively) were taken by optical interferometry, using a non-contact surface profiler as described by *Alshibli and Alsaleh* [2004] and *Morales et al.* [2009]. To avoid errors due to grain surface curvature and edges, only the center part of each grain was used for surface measurements. Surface topography data of naturally rough sand grains display significant differences in the peak to valley distance and location of surface asperities along the grain surface. In contrast, smoothed sand grains had an even asperity distribution with relatively small peak to valley distance from the mean grain surface.

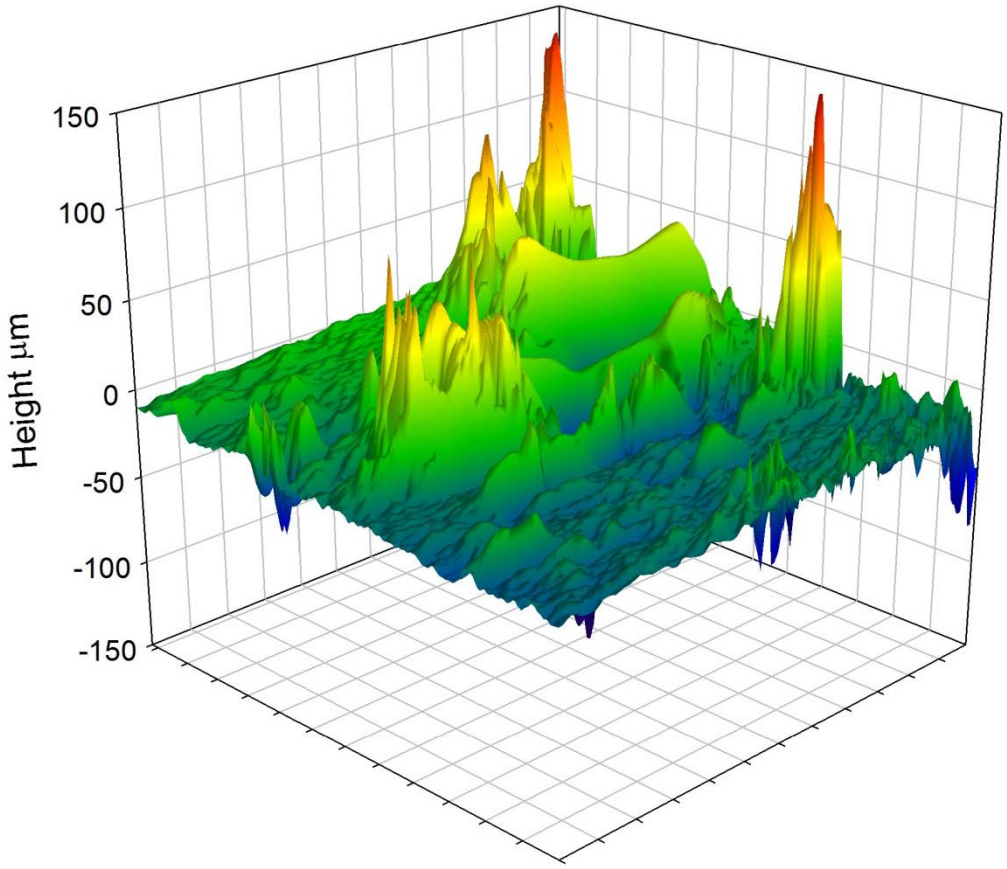

Figure A1. The surface topography of naturally rough sand grains

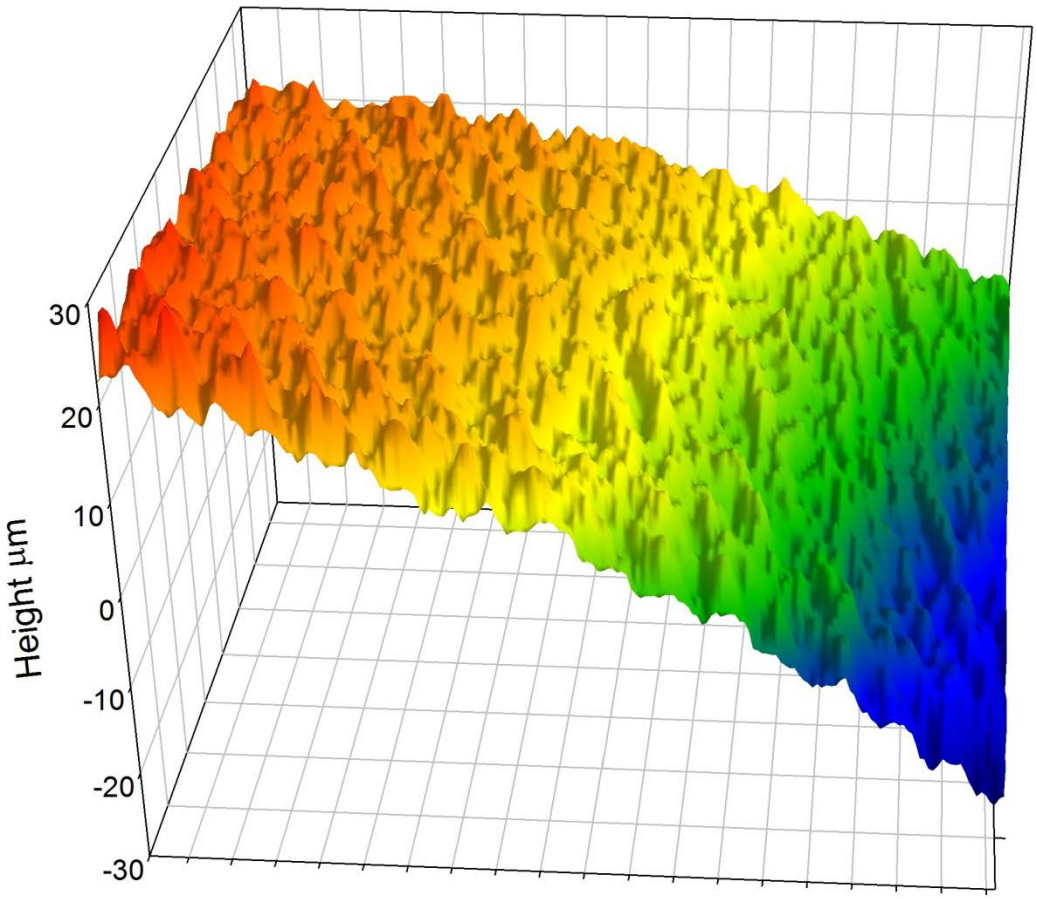

Figure A2. The surface topography of smoothed sand grains

A2. SUPPORTING VIDEOS

Videos showing the behaviors of colloids in pores (Videos 1 and 5) were taken by brightfield microscope at the same conditions used by *Zevi et al.*[2005] and *Zhang et al.* [2010], respectively. Videos including the detailed 3-D screen shot views of the simulations (Movies 2, 3, and 4) were taken by Cam Studio ®. Movies can be viewed and downloaded at http://soilandwater.bee.cornell.edu/colloids.html.